

Probing the initial conditions of high-mass star formation

III. Fragmentation and triggered star formation

Chuan-Peng Zhang^{1,2,3}, Tímea Csengeri³, Friedrich Wyrowski³, Guang-Xing Li^{4,5}, Thushara Pillai³, Karl M. Menten³, Jennifer Hatchell⁶, Mark A. Thompson⁷, and Michele R. Pestalozzi⁸

¹ National Astronomical Observatories, Chinese Academy of Sciences, 100101 Beijing, P.R. China
e-mail: cpzhang@nao.cas.cn

² Max-Planck-Institut für Astronomie, Königstuhl 17, D-69117 Heidelberg, Germany

³ Max-Planck-Institut für Radioastronomie, Auf dem Hügel 69, D-53121 Bonn, Germany

⁴ University Observatory Munich, Scheinerstrasse 1, D-81679 München, Germany

⁵ South-Western Institute for Astronomy Research, Yunnan University, Kunming, 650500 Yunnan, P.R. China

⁶ School of Physics, University of Exeter, Stocker Rd, Exeter EX4 4QL, United Kingdom

⁷ Centre for Astrophysics Research, University of Hertfordshire, College Lane, Hatfield, Herts AL10 9AB, United Kingdom

⁸ Istituto di Fisica dello Spazio Interplanetario - INAF, via Fosso del Cavaliere 100, 00133, Roma, Italy

Received XXX, XXX; accepted XXX, XXX

ABSTRACT

Context. Fragmentation and feedback are two important processes during the early phases of star formation.

Aims. Massive clumps tend to fragment into clusters of cores and condensations, some of which form high-mass stars. In this work, we study the structure of massive clumps at different scales, analyze the fragmentation process, and investigate the possibility that star formation is triggered by nearby H II regions.

Methods. We present a high angular resolution study of a sample of massive proto-cluster clumps G18.17, G18.21, G23.97N, G23.98, G23.44, G23.97S, G25.38, and G25.71. Combining infrared data at 4.5, 8.0, 24, and 70 μm , we use few-arcsecond resolution radio- and millimeter interferometric data taken at 1.3 cm, 3.5 mm, 1.3 mm, and 870 μm to study their fragmentation and evolution. Our sample is unique in the sense that all the clumps have neighboring H II regions. Taking advantage of that, we test triggered star formation using a novel method where we study the alignment of the centres of mass traced by dust emission at multiple scales.

Results. The eight massive clumps, identified based on single dish observations, have masses ranging from 228 to 2279 M_{\odot} within an effective radius of $R_{\text{eff}} \sim 0.5$ pc. We detect compact structures towards six out of the eight clumps. The brightest compact structures within infrared bright clumps are typically associated with embedded compact radio continuum sources. The smaller scale structures of $R_{\text{eff}} \sim 0.02$ pc observed within each clump are mostly gravitationally bound and massive enough to form at least a B3-B0 type star. Many condensations have masses larger than 8 M_{\odot} at small scale of $R_{\text{eff}} \sim 0.02$ pc. We find that the two lowest mass and lowest surface density infrared quiet clumps with $< 300 M_{\odot}$ do not host any compact sources, calling into question their ability to form high-mass stars. Although the clumps are mostly infrared quiet, the dynamical movements are active at clump scale (~ 1 pc).

Conclusions. We studied the spatial distribution of the gas conditions detected at different scales. For some sources we find hints of external triggering, whereas for others we find no significant pattern that indicates triggering is dynamically unimportant. This probably indicates that the different clumps go through different evolutionary paths. In this respect, studies with larger samples are highly desired.

Key words. Stars formation – techniques interferometer – ISM clouds – methods: observational

1. Introduction

High-mass stars are well-known to form as part of stellar clusters (e.g., Motte et al. 2018), in which they are greatly outnumbered by their low-mass cousins. Thus, the formation mechanism for individual high-mass stars is closely related to the formation and evolution of star clusters, which begins with the gravitational collapse of dense gas clumps of a parsec scale.

Observing the density structure of collapsing dense clumps is very important for our understanding of the star formation process. The radial density profile holds information concerning how collapse occurs (Larson 1969; Penston 1969; Shu 1977; Vázquez-Semadeni et al. 2009; Ballesteros-Paredes et al. 2011; Girichidis et al. 2014; Naranjo-Romero et al. 2015; Donkov & Stefanov 2018; Li 2018), and the masses and densities of the fragments hold clues to how high-mass stars form (McKee &

Tan 2002, 2003; Myers 1998; Padoan & Nordlund 2002; Bonnell et al. 2001; Klessen & Burkert 2001; Bonnell & Bate 2002; Bonnell et al. 2004). The observed fragments might also exhibit interesting spatial patterns: the fragments within a cluster often align along filamentary structures, e.g. G29.96e (Pillai et al. 2011), G28.34+p1 (Zhang et al. 2009) and G11.11-p1 (Wang et al. 2011, 2014). In short, constraining the number of fragments, their masses, and densities is fundamental to understanding how high-mass stars form.

Triggered star formation is still an open question, since the role and the mechanism of external influence on the collapse process is unclear. Several potential mechanisms exist, including “Collect and collapse” (Whitworth et al. 1994; Dale et al. 2007), and “radiatively driven implosion” (Sandford et al. 1982). In “collect and collapse”, during the expansion of an H II re-

Table 1. Parameters of PdBI observations.

Source	ATLASGAL name	Phase center (J2000)		3.5mm beam & rms		1.3mm beam & rms		Observational date							
		h	m	s	°	'	"		"	×	"	°	mJy/beam	"	×
CD configuration observations															
G18.17	G018.1750-0.2985	18 25 07.534	-13 14 32.75	4.75 × 2.48; 21.27	0.23	2.46 × 0.97; 19.98	1.67	Mar.25 – Apr.5, 2005							
G18.21	G018.2150-0.3419	18 25 21.558	-13 13 39.56	4.94 × 2.72; 18.23	0.20	2.47 × 0.99; 19.15	1.81	Mar.25 – Apr.5, 2005							
G23.97N	G023.9655+0.1382	18 34 28.833	-07 54 31.76	4.10 × 2.82; 21.58	0.32	1.85 × 1.07; 20.51	1.62	Mar.28 – Apr.6, 2005							
G23.98	G023.9790+0.1498	18 34 27.823	-07 53 28.76	4.23 × 2.95; 19.05	0.22	1.85 × 1.09; 20.89	1.65	Mar.28 – Apr.6, 2005							
G23.44	G023.4366-0.1828	18 34 39.253	-08 31 36.23	4.34 × 2.91; 20.48	0.25	1.89 × 1.05; 19.83	2.17	Mar.28 – Apr.6, 2005							
G23.97S	G023.9647-0.1094	18 35 22.160	-08 01 26.53	4.24 × 2.68; 21.68	0.23	1.93 × 1.01; 20.63	1.43	Mar.29 – Apr.12, 2005							
G25.38	G025.3826-0.1476	18 38 08.108	-06 46 54.93	4.18 × 2.82; 21.85	0.39	1.76 × 1.03; 21.27	1.34	Mar.29 – Apr.12, 2005							
G25.71	G025.7099+0.0448	18 38 03.184	-06 24 14.30	4.20 × 2.83; 22.82	0.26	1.89 × 1.05; 22.19	1.34	Mar.29 – Apr.12, 2005							
BCD configuration observations															
G23.44	G023.4366-0.1828	18 34 39.253	-08 31 36.23	2.20 × 1.54; 19.62	0.13	0.82 × 0.57; 17.32	0.75	Mar.14, Mar.16, 2006							
G23.97S	G023.9647-0.1094	18 35 22.160	-08 01 26.53	2.16 × 1.53; 22.87	0.13	0.83 × 0.59; 26.90	0.64	Mar.14, Mar.16, 2006							
G25.38	G025.3826-0.1476	18 38 08.108	-06 46 54.93	2.17 × 1.55; 22.66	0.20	0.78 × 0.60; 23.19	0.66	Feb.27, Mar.17, 2006							
G25.71	G025.7099+0.0448	18 38 03.184	-06 24 14.30	2.21 × 1.54; 24.73	0.16	0.83 × 0.58; 24.19	0.66	Feb.27, Mar.17, 2006							

gion, the diffuse gas surrounding it is collected into dense structures which then collapse (Zhang et al. 2013, 2016). In “radiatively driven implosion”, pre-existing overdensities in the molecular gas are enhanced when an ionization front sweeps away the less dense gas and begins to compress the overdensities from all sides, inducing collapse (Henney et al. 2009). H II regions interact with their neighboring molecular clouds by pushing away the lower density material faster than the higher density cloud cores embedded inside (Zhang & Wang 2012). This may lead to bright rims and pillars (Klein et al. 1980; Sugitani et al. 1989; Elmegreen 2011). However, it is still unclear how important these processes are for the gravitational collapse of the clumps and the subsequent star formation. In this paper, we address this question using a novel method where we study the alignment of the centre of mass traced by dust emission at multiple scales.

Kauffmann & Pillai (2010) defined an empirical threshold of $m(r) > 870 M_{\odot} (r/\text{pc})^{1.33}$ for massive star formation, where $m(r)$ is the clump mass and the effective radius $r = \text{FWHM}/(2\sqrt{\ln 2})$. In our previous work (Zhang & Li 2017), we have presented the *mass-size* relations for all clumps, cores, and condensations at 3.5 mm, 1.3 mm, 870 μm , 850 μm , and 450 μm . We found that our samples are potential intermediate- or high-mass star-forming candidates. We fit these parameters using a power law that yields $M \propto r^{1.68}$. Li (2017) predict that if the ambient turbulence is characterised by a constant energy dissipation rate ϵ , gravitationally bound structures will follow $M \approx \epsilon^{2/3} \eta^{-2/3} G^{-1} r^{5/3}$, where η is a parameter for turbulent dissipation, and is close to unity, G is the gravitational constant, and r is the size. Thus the *mass-size* scaling is determined by the energy dissipation rate ϵ . When ϵ is a constant through the medium, $M \propto r^{5/3} \propto r^{1.67}$. Therefore, our observational results support a scenario where molecular gas in the high-mass star formation regions is supported by turbulence with an almost constant energy dissipation rate, and gas fragments like clumps and cores are structures which are dense enough to be dynamically detached from the ambient medium. A more detailed discussion is presented in Li (2017) and Zhang & Li (2017).

In this work, we adopt a commonly used terminology for clumps, dense cores, and condensations having a physical FWHM size of ~ 1 , ~ 0.1 , and ~ 0.01 pc, respectively (Williams et al. 2000; Wang et al. 2014; Pokhrel et al. 2018). Based on the derived effective radii of our sample, we thus refer to the objects observed with single-dish telescopes at 450, 850, and 870 μm observations as clumps, the objects in the 1.3 cm VLA observations and in the 3.5 and 1.3 mm PdBI CD configuration ob-

servations as cores, and the objects in the 3.5 and 1.3 mm PdBI BCD configuration observations as condensations (see datasets in Section 2). We report the fragmentation properties of eight high-mass star-forming regions, some of which are infrared quiet suggesting that they are in an early evolutionary stage. In Section 2, we describe the sample selection. In Section 3, we list observational results at different scales and different wavelengths. In Section 4, infrared extinction, clump extraction, and kinetic temperature are presented and analyzed. In Section 5, we mainly discuss dynamics, virial stability, fragmentation features, evolutionary stages, and potential triggered star formation of the clumps. In Section 6, we give a summary.

2. Observations and data reduction

2.1. SCAMPS sources — sample selection

Eight massive clumps (G18.17, G18.21, G23.97N, G23.98, G23.44, G23.97S, G25.38, and G25.71) were selected from the SCUBA Massive Pre/Protocluster core Survey (SCAMPS; Thompson et al. 2005; Pillai et al. 2007). The SCAMPS survey takes a wide-field ($10' \times 10'$) census of clouds in 32 high-mass star-formation regions at 850 μm and 450 μm with James Clerk Maxwell Telescope (JCMT). The rationale behind the SCAMPS strategy is that, as high-mass stars are found in clusters and many ultra-compact (UC) H II regions are located in clusters, one expects to find even earlier phases of massive star formation in the vicinity of such UC H II regions. In addition, as sub-millimeter continuum emission is optically thin and sensitive to both warm and cold dust, it provides an unbiased census of all massive pre- and protocluster clumps in the vicinity of the already formed massive young stellar objects (YSOs). The parameters including coordinates, observational dates, and distances of the selected eight clumps are listed in Table 1 and Table 3. The observational parameters of the clumps at 850 and 450 μm are listed in Table D.1.

2.2. ATLASGAL sources

These eight massive clumps were also identified in the Atacama Pathfinder Experiment (APEX) Telescope Large Area Survey of the Galaxy (ATLASGAL¹; Schuller et al. 2009). The survey was

¹ The Atacama Pathfinder Experiment (APEX) project is a collaboration between the Max-Planck-Gesellschaft, the European Southern Observatory (ESO) and the Universidad de Chile.

Table 2. Parameters of VLA observations.

Source	Phase center (J2000)		NH ₃ (1,1) beam & rms	
	h	m s	° ' "	" × "; ° mJy/beam
D configuration				
G18.17	18 25 07.534	-13 14 32.75	4.61 × 3.24; 13.50	~3.3
G18.21	18 25 21.558	-13 13 39.56	4.64 × 3.24; 15.06	~3.6
G23.97N	18 34 28.833	-07 54 31.76	4.03 × 3.34; -5.64	~3.2
G23.98	18 34 27.823	-07 53 28.76	4.03 × 3.33; -7.06	~3.3
G23.44	18 34 39.253	-08 31 36.23	4.18 × 3.42; -7.07	~3.6
G23.97S	18 35 22.160	-08 01 26.53	4.04 × 3.34; -3.95	~2.8
G25.38	18 38 08.108	-06 46 54.93	4.10 × 3.41; -7.48	~2.6
G25.71	18 38 03.184	-06 24 14.30	4.06 × 3.43; -6.29	~2.6

carried out at 870 μm with a resolution of 19.2", and has a goal of investigating massive clumps associated with high-mass star-forming regions. ATLASGAL has been described in detail by Csengeri et al. (2014); Urquhart et al. (2014). The observational parameters of the clumps at 870 μm are listed in Table D.1.

2.3. PdBI observations

The eight clumps were observed with the IRAM² Plateau de Bure Interferometer (PdBI) in the 3.5 and 1.3 mm simultaneously during 2004 and 2006. The 3.5 mm receivers were tuned to 86.086 GHz in single sideband (SSB) mode. The 1.3 mm receivers were tuned to 219.560 GHz in double sideband (DSB) mode. Both receivers used two 320 MHz wide backends for continuum observation. In addition, we also obtained data for five molecular lines, i.e., NH₂D (85.926 GHz), HC¹⁵N (86.055 GHz), SO (86.094 GHz), H¹³CN (86.340 GHz), and C¹⁸O (219.560 GHz) with narrow correlator windows affording adequate high spectral resolution. The spectral data will be presented in a forthcoming paper.

For the clumps G18.17, G18.21, G23.97N, G23.98, G23.44, G23.97S, G25.38, and G25.71, the observations were first carried out with both C and D configurations between March and April 2005. The typical synthesized beam size for CD configuration observation is about 4.2" × 2.8" at 3.5 mm and 1.8" × 1.0" at 1.3 mm. Then, the four brightest clumps (G23.44, G23.97S, G25.38, and G25.71) were observed again in the B configuration between February and March 2006. The typical synthesized beam size for images produced from the combined C+D configuration data is about 4.2" × 2.8" at 3.5 mm and 1.8" × 1.0" at 1.3 mm. The typical synthesized beam size for images produced from the combined B+C+D configuration data is about 2.2" × 1.5" at 3.5 mm and 0.8" × 0.6" at 1.3 mm. For calibrations, the quasar B1741-038 was used as phase calibrator, and the quasar 3C273 and the evolved star MWC 349 were used as absolute flux calibrators.

The CLIC and MAPPING modules in the IRAM software package GILDAS³ were used for the data calibration and image processing. The uv -tables from the line-free channels were imaged and cleaned to obtain continuum images with uniform weighting to optimize spatial resolution for G18.17, G18.21, G23.44, G23.97S, G25.38, and G25.71, and with natural weighting to increase the signal to noise ratio for G23.97N and G23.98. A region twice the size of primary beam was imaged. Clean components were searched in the whole image without using a cleaning mask. The primary beam is 58.5" at 86.086 GHz, and 23.0" at 219.560 GHz, respectively. The images were corrected

for primary beam attenuation. The phase center, beam size, and rms noise of the images not corrected for primary beam response are listed in Table 1.

2.4. VLA observations

The same eight clumps were also observed at 1.3 cm with NRAO⁴ Very Large Array (VLA) D-configuration on November 2005 (project ID AW0669). The spectra $J, K = (1, 1)$ and $(2, 2)$ transitions of NH₃ were simultaneously covered, using the 2-IF spectral line mode of the correlator, with 6.25 MHz bandwidth and 127 channels of width 49 kHz (0.617 km s⁻¹) each. The NH₃ (1, 1) and (2, 2) transitions have five and three hyperfine structure (HFS) lines, respectively, and the frequencies of the strongest HFS lines are at 23.694 and 23.723 GHz, respectively. Due to the narrow bandwidth of 6.25 MHz at around 23.7 GHz, it can just cover at most four HFS lines in five of NH₃ (1, 1). The primary beam is about 2', and the typical synthesized beam size is about 3.0" × 2.5" at 1.3 cm. The spectra and continuum were calibrated with primary beam correction.

The raw data was exported to MIRIAD⁵ for calibration. The absolute flux calibrator was J1331+305, the antenna gain and phase calibrator was B1743-038, and the bandpass calibrator was J1256-057. The phase centers were the same as for the PdBI observations, listed in Table 1. Natural weighting was used for data calibration and cleaning. The whole primary beam was imaged and cleaned. No polygon was introduced to avoid any biased cleaning.

With the MIRIAD software, we summed up the line-free channels to produce a "pseudo" continuum database which was subtracted from the uv -data in the uv -plane. The line-free continuum was self-calibrated, and the gain solutions were applied to the spectral line data. The image data cubes were exported to CLASS and GREG in GILDAS for further continuum and spectral line analysis. The phase center, beam size, and rms noise of the images not corrected for primary beam response are listed in Table 2.

3. Results

3.1. Clumps on large scale

In Figure 1(a), we present the large-scale emission of the clumps as imaged by APEX ATLASGAL at 870 μm (see also Figures D.1(a) to D.7(a) in Appendix). The 870 μm emission is an excellent tracer of cool and dense gas. Each peak position of the

² IRAM is supported by INSU/CNRS (France), MPG (Germany) and IGN (Spain).

³ <http://www.iram.fr/IRAMFR/GILDAS/>

⁴ The National Radio Astronomy Observatory is a facility of the National Science Foundation operated under cooperative agreement by Associated Universities, Inc.

⁵ <http://www.cfa.harvard.edu/sma/miriad/>

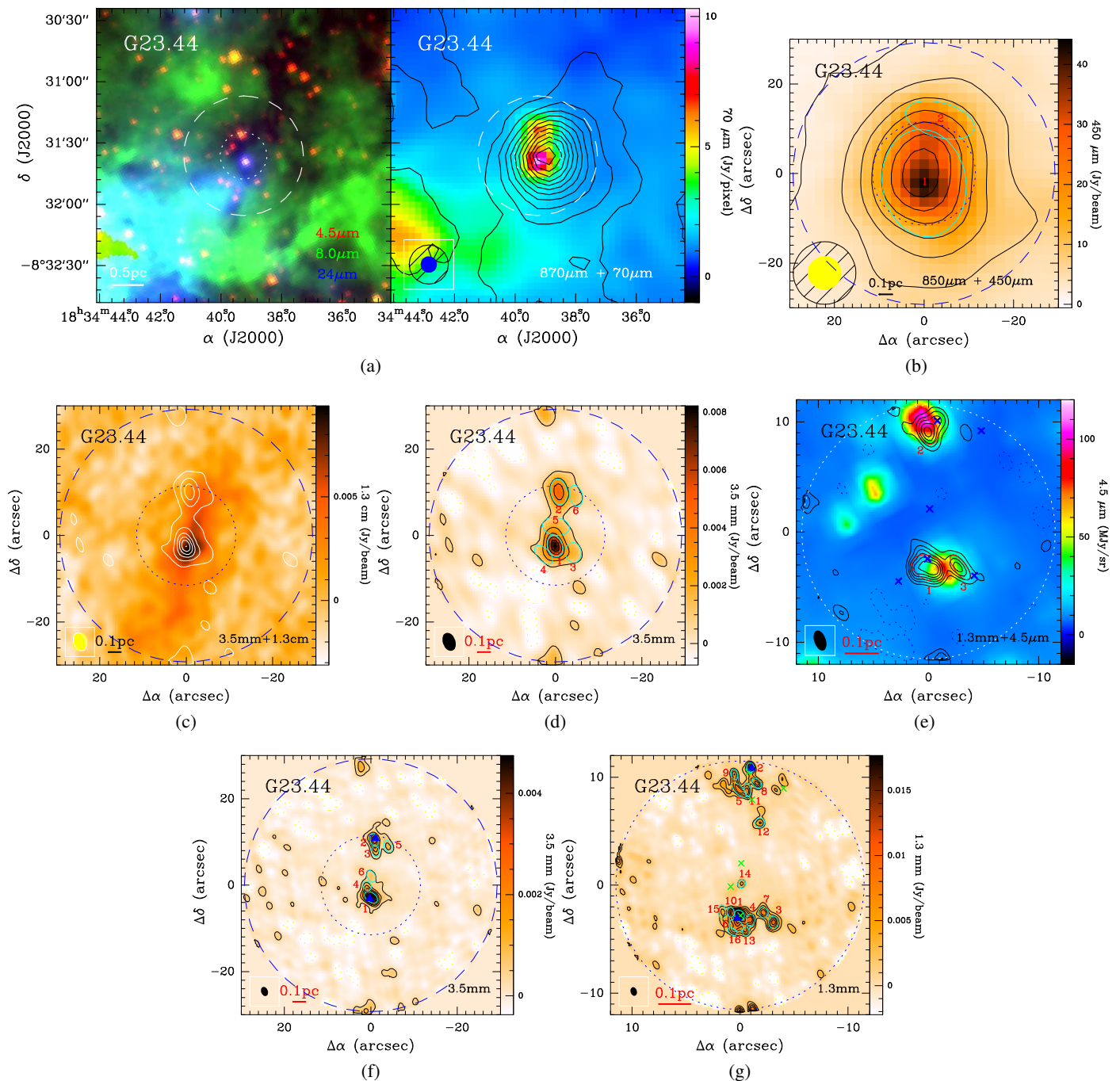


Fig. 1. G23.44: (a) (left) Three-color image of $4.5\ \mu\text{m}$ (blue), $8.0\ \mu\text{m}$ (green), and $24\ \mu\text{m}$ (red); (right) $870\ \mu\text{m}$ contours overlaid on a $70\ \mu\text{m}$ color scale. The $870\ \mu\text{m}$ contour levels start at 6σ in steps of 10σ ($\sigma = 54\ \text{mJy beam}^{-1}$). (b) $850\ \mu\text{m}$ contours overlaid on a $450\ \mu\text{m}$ color scale. The $850\ \mu\text{m}$ contour levels start at 6σ in steps of 12σ ($\sigma = 83\ \text{mJy beam}^{-1}$). (c) $3.5\ \text{mm}$ contours overlaid on a $1.3\ \text{mm}$ color scale. For CD configuration observations, (d) the $3.5\ \text{mm}$ contour levels start at -3σ , 3σ in steps of 6σ ($\sigma = 0.25\ \text{mJy beam}^{-1}$), and (e) the $1.3\ \text{mm}$ contour levels start at -3σ , 3σ in steps of 2σ ($\sigma = 2.17\ \text{mJy beam}^{-1}$). For BCD configuration observations, (f) the $3.5\ \text{mm}$ contour levels start at -3σ , 3σ in steps of 4σ ($\sigma = 0.13\ \text{mJy beam}^{-1}$), and (g) the $1.3\ \text{mm}$ contour levels start at -3σ , 3σ in steps of 2σ ($\sigma = 0.75\ \text{mJy beam}^{-1}$) superimposed on a $24\ \mu\text{m}$ color scale. The ellipses with numbers indicate the positions of extracted sources. The crosses in the $1.3\ \text{mm}$ (B)CD configuration observations indicate the peak positions of the corresponding cores and condensations in the $3.5\ \text{mm}$ (B)CD configuration observations. The dashed and dotted circles in each subfigure indicate the primary beam scales of 3.5 and $1.3\ \text{mm}$ PdBI tracks, respectively. The blue triangle “▲” indicates the position of $6668\ \text{MHz}$ methanol masers. Versions of this figure for sources G18.17 (see Figure D.1), G18.21 (see Figure D.2), G23.97N (see Figure D.3), G23.98 (see Figure D.4), G23.97S (see Figure D.5), G25.38 (see Figure D.6), and G25.71 (see Figure D.7) are available online only.

$870\ \mu\text{m}$ emission is close to a strong UC H II region. We find that most of the UC H II regions have corresponding compact millimeter wavelength sources, detected at 870 , 850 , and $450\ \mu\text{m}$. The emission distributions at 870 , 850 , and $450\ \mu\text{m}$ have simi-

lar morphological correlations as shown in Figure 1(b) (see also Figures D.1(b) to D.7(b) in Appendix).

To measure the physical parameters of the clumps at different wavelengths, we used the `Gaussclumps` algorithm (Stutzki & Guesten 1990) to extract their peak positions, sizes,

Table 3. The properties of infrared data.

Source ^a	$S_{4.5\mu\text{m}}$ mJy	$S_{8.0\mu\text{m}}$ mJy	$S_{24\mu\text{m}}$ mJy	$S_{70\mu\text{m}}$ Jy	Infrared ^b	H II ^c	Distance kpc	Ref. for dist.
G18.17	1.3(0.2)	916.3(68.0)	214.9(56.6)	2.5(0.1)	quiet	no	3.73	1, 2
G18.21	13.6(0.8)	27.9(1.7)	773.3(14.2)	4.6(0.8)	quiet	no	3.60	1, 2
G23.97N	—	—	—	28.9(0.4)	quiet	no	4.68	1, 2
G23.98	4.9(0.6)	167.8(6.5)	8.7(2.6)	—	quiet	no	4.68	1, 2
G23.44-l	14.9(2.0)	34.3(0.2)	1683.5(165.5)	150.3(0.5)	bright	yes	5.88	3
G23.44-u	25.7(2.2)	23.6(0.2)	300.1(68.3)	115.6(0.5)	quiet	no	5.88	3
G23.97S	10.2(0.4)	5.6(0.8)	709.6(3.6)	179.8(0.4)	quiet ^d	yes ^d	4.70	1, 2
G25.38-l	45.7(0.5)	50.1(3.6)	252.3(38.6)	28.7(0.4)	quiet	no	5.60	4, 5, 6
G25.38-u	—	—	—	—	quiet	no	5.60	4, 5, 6
G25.71-l	154.4(2.0)	272.0(8.0)	6197.1(122.6)	399.9(0.6)	bright	yes	9.50	6, 7
G25.71-u	138.7(2.2)	2453.2(24.9)	16109.0(83.8)	182.3(0.5)	bright	yes	9.50	6, 7

Notes. ^(a) The “-l” and “-u” following source names indicate the lower and upper clusters (e.g. No.1 and No.2 at 3.5 mm in Figure 1(d)) in corresponding clumps. ^(b) Mainly based on a threshold of MIPS 24 μm flux $S_{24\mu\text{m}} = 15.0\text{ Jy}$ at a distance of 1.7 kpc (Motte et al. 2007), this flux limit can be rescaled to the distance of the sources in this table. ^(c) Compact H II region candidate, judged by whether there is a corresponding 1.3 cm continuum at its sensitivity. ^(d) G23.97S is actually associated with the very weak infrared source at the north of the bright one (see Figures D.5(e)), so it is an infrared quiet source. However, 1.3 cm continuum was detected so it belongs to an H II region.

References for distance. ⁽¹⁾ Wienen et al. (2012) ; ⁽²⁾ Reid et al. (2009) ; ⁽³⁾ Brunthaler et al. (2009) ; ⁽⁴⁾ Anderson & Bania (2009) ; ⁽⁵⁾ Ai et al. (2013) ; ⁽⁶⁾ Urquhart et al. (2013) ; ⁽⁷⁾ Lockman (1989) .

and peak fluxes (see details in Section 4.1). We take $R_{\text{eff}} = \text{FWHM}/(2\sqrt{\ln 2})$ as the source effective radius, where FWHM is the Gaussian source size. The effective radii R_{eff} of the clumps range from 0.17 to 0.89 pc (see Table D.1). Based on these measurements, we further derived other parameters including integrated flux, mass and density, shown in Table D.1. The fitted FWHMs at 450 μm are indicated with green ellipses in Figure 1(b).

3.2. Cores and condensations on small scale

From the sizes and masses measured at 870, 850, and 450 μm (Table D.1), we expect these clumps are candidate hosts of forming or recently formed high mass stars. To unveil the population of dense cores, we show the higher angular resolution observations at 3.5 and 1.3 mm with the B, C, and D configurations of PdBI in Figures 1(d)(e). The physical parameters of the cores at the 3.5 and 1.3 mm are listed in Tables D.2 and D.3. The derived effective radii R_{eff} of the cores and condensations range from 0.027 to 0.102 pc (see Table D.2), and from 0.010 to 0.044 pc (see Table D.3), respectively.

At the current sensitivity and $\sim 1\text{--}2''$ resolution, the clumps G18.17, G18.21, G23.97N, and G23.98 are probably resolved, as they only host isolated and weak cores at 1.3 mm. However, clumps G23.44, G23.97S, G25.38, and G25.71 show compact structures and high flux densities in the CD configuration data. It is likely that these observations have not completely resolved these densest cores. Based on this, the higher angular resolution BCD configuration observations were used to investigate these four sources further.

In Figures 1(f)(g), we show the small-scale fragmented condensations as imaged from the 3.5 and 1.3 mm BCD configuration data towards clump G23.44 (see also clumps G23.97S, G25.38, and G25.71 in Appendix Figures D.5(f)(g), D.6(f)(g), and D.7(f)(g), respectively). The best mass sensitivity is $0.5 M_{\odot}$ with a spatial scale of about 2063 AU corresponding to the source G23.97S-6 (see Table D.3) in these observations. The physical parameters determined from these data are also listed in Tables D.2 and D.3. The clumps fragment further at this higher resolution into clusters of small cores and condensations. The densest and most massive condensations are potential candidate

hosts of high-mass protostars. We will further investigate their chemistry, dynamics, and luminosity in a forthcoming work. Their physical parameters, such as mass, size, and density, will be analyzed in the following sections.

4. Analysis

4.1. Clump, core, and condensation extractions

Assuming that the flux density of each sub-source is approximated by a Gaussian distribution, the Gaussclumps procedure (Stutzki & Guesten 1990; Kramer et al. 1998) in the GILDAS software package was used to characterize clumps, cores, and condensations at all different scales and wavelengths in our sample. We consider sources with peak intensity above 5σ before primary beam correction. The derived parameters are listed in Tables D.1, D.2, and D.3. Their statistics shows that 27 and 18 compact sources were identified in the eight clumps in the 3.5 and 1.3 mm CD configuration observations, respectively. This gives on average 3.4 and 2.3 sources per clump corresponding to a population of cores and condensations, respectively, similar to that observed in high-mass clumps by Csengeri et al. (2017). Despite their prominent peak at 870 μm , towards the clumps G23.97N, and G23.98 we do not find strong compact continuum sources at 3.5 and 1.3 mm. While G23.97N may host a relatively weak single source, the G23.98 field is devoid of compact sources.

4.2. Infrared emission

The earliest phase of (high-mass) star formation takes place in cold and dense material, prior to the appearance of luminous embedded objects. (Near) Infrared emission which traces warm dust is a useful tool to study the evolution at these early phases. We investigated objects associated with our sample of clumps by combining infrared data including the GLIMPSE 4.5 μm , 8.0 μm (Benjamin et al. 2003; Churchwell et al. 2009), MIPS-GAL 24 μm (Carey et al. 2009; Gutermuth & Heyer 2015), and PACS (or Hi-GAL) 70 μm (Poglitsch et al. 2010; Molinari et al. 2016; Marton et al. 2017) images and catalogs. For the sources not available in the archival catalogs, we used aperture photom-

entry in the MOsaicker and Point source EXtractor (MOPEX) package (Makovoz & Marleau 2005) to compute fluxes (listed in Table 3) at 4.5, 8.0, 24, and 70 μm . Using these measurements, we followed the criteria of Motte et al. (2007) and Russell et al. (2010) (towards Cygnus X and NGC 6334 – NGC 6357, respectively) for identifying infrared bright and quiet point sources based on the MIPS GAL 24 μm images. We scaled the flux density threshold of $S_{24\mu\text{m}} = 15.0 \text{ Jy}$ at a distance of 1.7 kpc (Motte et al. 2007) to the distances of our sources as $S_{24\mu\text{m}} < (\frac{1.7 \text{ kpc}}{D})^2 \times 15.0 \text{ Jy}$ to identify infrared quiet clumps, where D is the distances of our sources, and $S_{24\mu\text{m}}$ is the flux density obtained from the MIPS GAL survey, as listed in Table 3. We find that most of the sources fall below the infrared quiet criterion, but four clumps are infrared bright (see also Figures D.1(a) to D.7(a)). Point-source like emission at 70 μm is also a reasonably good indicator of embedded YSOs. Using the Hi-GAL 70 μm data (Molinari et al. 2016), we find that roughly half of the sources are associated with bright 70 μm point sources, while the clumps G23.98 and G25.38-u do not host any 70 μm point source. This suggests that star formation may be active in the infrared bright cores within some of the clumps. We discuss the infrared features of individual clumps in Appendix C.

The saturated infrared emission seen in Figure 1(a) originates from the neighboring UC H II regions that are in the vicinity of our targets (see also Section 2.1). These certainly harbor more evolved objects than our source sample, and in Section 5.6 we test whether feedback from these (UC-)H II regions influences the evolution of our targets.

4.3. Kinetic temperature

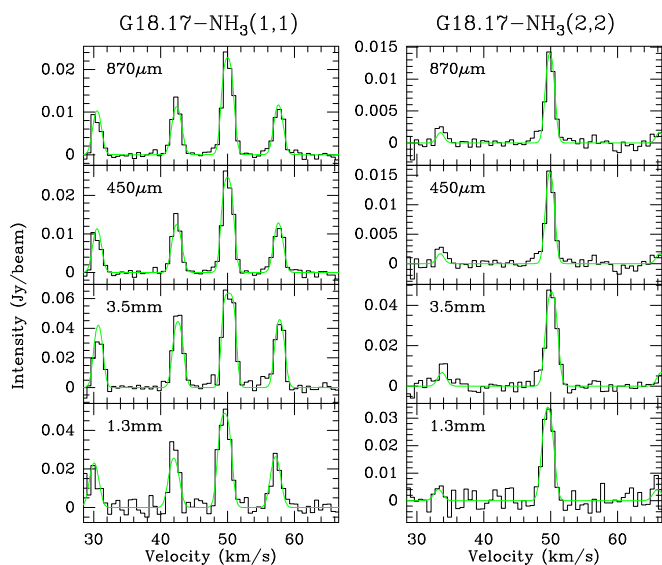


Fig. 2. NH_3 (1, 1) and (2, 2) example spectra overlaid with their HFS fits for the fragment G18.17-No.1 (see Tables D.1, D.2, and D.3). Top to bottom: the lines are averaged within different fragment scales, respectively, at 870 μm , 450 μm , 3.5 mm (CD configuration observations), and 1.3 mm (CD configuration observations).

The rotational temperature of the ammonia transitions was estimated using the ratio of the brightness temperatures between the NH_3 (1, 1) and (2, 2) transitions (e.g., Figures 2, and 3), along with the NH_3 (1, 1) optical depth following Ho & Townes (1983). The optical depths of NH_3 (1, 1) were derived from fitting the hyperfine structure (HFS) lines and obtaining the ratio

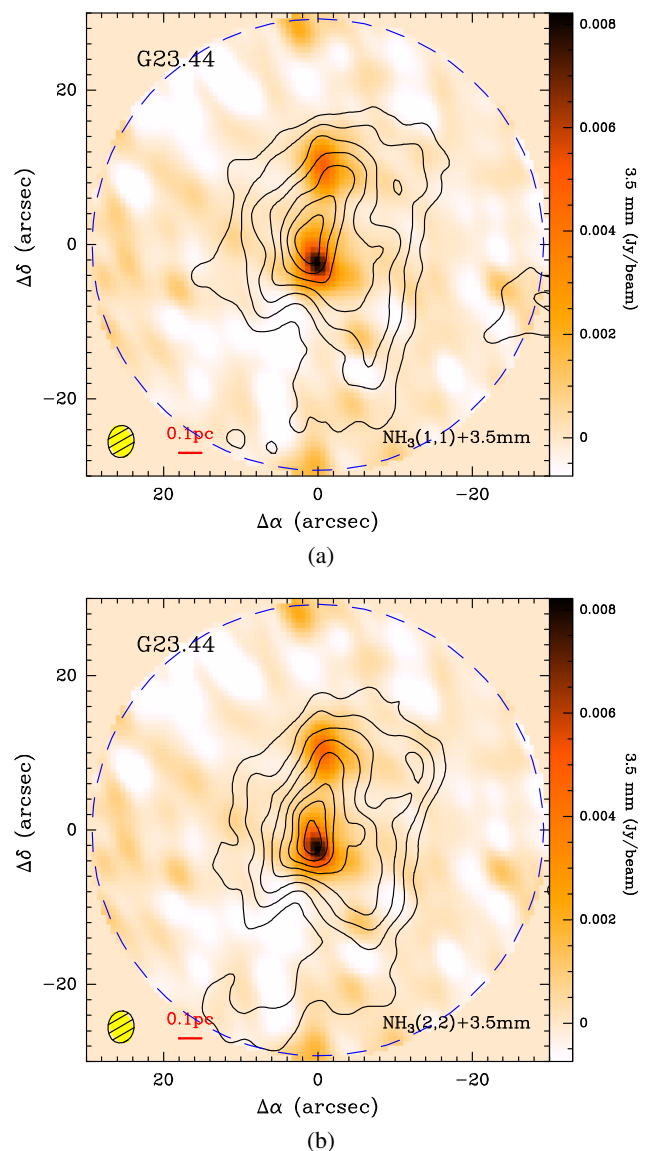


Fig. 3. NH_3 (1, 1) and (2, 2) integrated-intensity contours overlaid on a 3.5 mm continuum with velocity range covering only the main line, respectively. The contour levels start at -3σ in steps of 3σ for NH_3 (1, 1) with $\sigma = 15.8 \text{ mJy beam}^{-1} \text{ km s}^{-1}$ and NH_3 (2, 2) with $\sigma = 12.3 \text{ mJy beam}^{-1} \text{ km s}^{-1}$. The synthesized beam size of each subfigure is indicated at the bottom-left corner. Other sources are presented in Figures D.8 and D.9.

of the main to the satellite line strengths. Considering that the extracted sources have different scales, we average these spectra of NH_3 (1, 1) and (2, 2) within the measured Gaussian FWHM of each source to get a high signal to noise ratio spectrum.

The kinetic temperature T_{kin} can be estimated from the rotational temperature T_{rot} derived using NH_3 (1, 1) and (2, 2) transitions. Based on large velocity gradient (LVG) calculations, Ott et al. (2011) provide a reasonable approximation for the conversion from T_{rot} to T_{kin} as

$$T_{\text{kin}} = 6.06 \times e^{0.061T_{\text{rot}}}. \quad (1)$$

The derived kinetic temperatures are listed in Tables D.1, D.2, and D.3. The kinetic temperature maps overlaid by 3.5 mm continuum contours are presented in Figure 4. The temperatures range from 12.5 to 63.1 K with mean and median of 28.3 and 23.6 K, respectively. Only 10.2% of all sources have kinetic

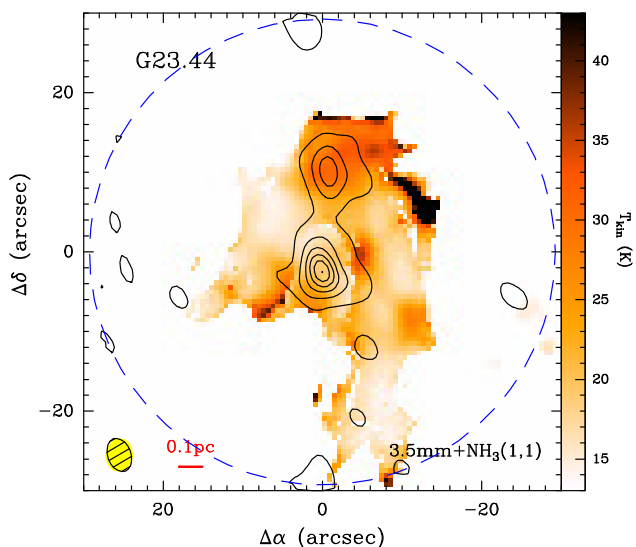


Fig. 4. The kinetic temperature T_{kin} maps overlaid by 3.5 mm continuum contours. The 3.5 mm contour levels start at 3σ in steps of 6σ ($\sigma = 0.25 \text{ mJy beam}^{-1}$). The synthesized beam size is indicated at the bottom-left corner. Other sources are presented in Figure D.10.

temperatures above 40 K. Such high temperatures are observed mainly towards the cores associated with compact H II regions in clumps G23.44 and G23.97S⁶. Furthermore, it is obvious that the obtained rotational temperatures at large scale are lower than those at small scale.

4.4. Mass and density calculations

It is assumed that the dust emission is optically thin and the gas to dust ratio is 100 by mass. For all clumps, cores, and condensations, we adopt the kinetic temperatures derived from their rotational temperatures between $\text{NH}_3(1,1)$ and $(2,2)$ as an approximate dust temperature (see Section 4.3). The source masses are calculated using dust opacities of $0.002 \text{ cm}^2 \text{ g}^{-1}$ at 3.5 mm and $0.009 \text{ cm}^2 \text{ g}^{-1}$ at 1.3 mm for thin ice mantles at a gas density of 10^6 cm^{-3} (Ossenkopf & Henning 1994; Pillai et al. 2011). In addition, dust opacities of 0.0185, 0.0182, and $0.0619 \text{ cm}^2 \text{ g}^{-1}$ are adopted for 870, 850, and $450 \mu\text{m}$, respectively (Ossenkopf & Henning 1994). The total mass M of each source can therefore be calculated (Kauffmann et al. 2008) via

$$\left(\frac{M}{M_{\odot}}\right) = 0.12 \left(e^{14.39 \left(\frac{\lambda}{\text{mm}}\right)^{-1} \left(\frac{T_{\text{dust}}}{\text{K}}\right)^{-1}} - 1 \right) \times \left(\frac{\kappa_{\nu}}{\text{cm}^2 \text{ g}^{-1}}\right)^{-1} \left(\frac{S_{\nu}}{\text{Jy}}\right) \left(\frac{D}{\text{kpc}}\right)^2 \left(\frac{\lambda}{\text{mm}}\right)^3, \quad (2)$$

where λ is the observational wavelength, T_{dust} is the dust temperature, κ_{ν} is the dust opacity, S_{ν} is the integrated flux, and D is the distance to the Sun. Moreover, the column density, volume density and surface density are derived as $N_{\text{H}_2} \sim M/\text{FWHM}^2$, $n_{\text{H}_2} \sim M/\text{FWHM}^3$, and $\Sigma = M/(\pi R_{\text{eff}}^2)$, respectively, where $R_{\text{eff}} = \text{FWHM}/(2\sqrt{\ln 2})$ is the source effective radius, and FWHM is the Gaussian source size. These corresponding parameters are listed in Tables D.1, D.2, and D.3. The mass uncer-

⁶ Ammonia is not a good probe of the material close to the heating source; instead it shows the conditions in the outer layer of the envelope. Therefore, the temperatures in clumps containing compact H II regions may be underestimated.

tainties are mainly derived by error propagation from the rotational temperature. Considering the interferometric filtering, the derived masses are lower limits.

In addition, we distinguish the contribution from the dust and the free-free emission at 3.5 mm based on the SED fitting for the clumps G23.44, G23.97S, G25.38, and G25.71 (see Section A and Fig. A.1 in Appendix). For the most massive objects within the clumps G18.17, G18.21, G23.97N, and G23.98, the expected free-free emission level at 3.5 mm is at least half orders of magnitude lower than the detected dust emission at 3.5 mm according to these detection limits at 6 and 1.3 cm, therefore, we assume that their measured integrated fluxes are purely from dust emission.

In Table D.1, there is some difference among the masses derived from 870, 850, and $450 \mu\text{m}$. While the flux calibration errors are similar at each wavelength, the measured Gaussian traces from GaussClumps are different as different wavelengths trace different scales and structures. In this work, we adopt the masses and sizes derived mainly at $870 \mu\text{m}$ for further investigation.

5. Discussion

5.1. Gas dynamics

Gas dynamics shapes the morphology of molecular clouds at large scale, and plays a major role in stabilizing the entire core against fragmentation (Csengeri et al. 2011a,b; Naranjo-Romero et al. 2015). Molecular clouds in early stage often exhibit complex gas dynamical phenomena, such as outflow, rotation, convergent flow, and collision (Schneider et al. 2010; Zhang et al. 2009; Beuther et al. 2013; Zhang et al. 2017a).

$\text{NH}_3(1,1)$ is a good tracer of relatively diffuse and extended molecular clouds, and often used as dynamical tracer (e.g., Galván-Madrid et al. 2009; Zhang et al. 2014). In Figure 5, we present velocity distributions (moment 1) of $\text{NH}_3(1,1)$. It is very obvious that there exists a steep velocity gradient for the eight molecular clumps, such as G18.17 and G23.97N in east-west direction, G23.44, G25.38, and G25.71 in north-south direction, and the other sources (G23.98 and G23.97S) having two velocity components crossing into together. It is likely that the molecular clumps are colliding each other, or simply overlapping in the plane of the sky but are physically separated in the third spatial dimension. We also present velocity dispersion (moment 2) of $\text{NH}_3(1,1)$ line. We found that the 3.5 mm emission is associated with the dynamically dominated regions. In general, the dynamical movements are active at clump scale ($\sim 1 \text{ pc}$), although most of the central cores are in a very early stage.

5.2. Virial stability

The virial theorem can be used to test whether a source is unstable to collapse. To apply the virial theorem, a density profile needs to be specified. We assume a simple spherical source with a density distribution of $\rho \propto r^{-2}$ (e.g., Shu 1977), which we take as an indication that self-gravity is dominating the collapse (Li 2018). There are a few previous explanations of this profile: according to Shu (1977), an initial density profile of $\rho \propto r^{-2}$ is established before protostellar collapse due to pressure support, and a somewhat shallower density profile is established at the center after the formation of the protostar. The r^{-2} profile in Shu (1977) is hydrostatic in nature and exhibits zero infall. This is contradicted by the fact that clumps like ours typically show some degree of infall. It has also been argued that a free-fall collapse can produce such a steep density pro-

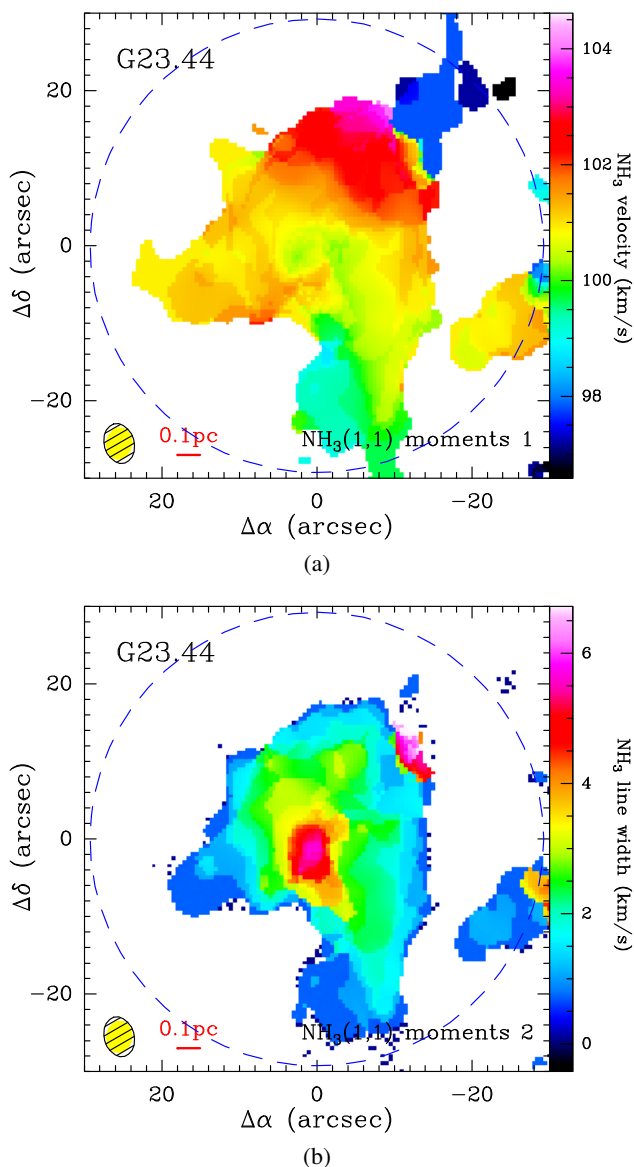


Fig. 5. (a) Velocity distribution (moment 1) and (b) velocity dispersion (moment 2) of NH_3 (1, 1) line. The synthesized beam size of each sub-figure is indicated at the bottom-left corner. Other sources are presented in Figures D.11 and D.12.

file (Larson 1969; Penston 1969; Vázquez-Semadeni et al. 2009; Ballesteros-Paredes et al. 2011; Girichidis et al. 2014; Naranjo-Romero et al. 2015; Donkov & Stefanov 2018) and the infall velocity is also close to the free-fall velocity (Murray & Chang 2015). One might be tempted to interpret the r^{-2} profile using free-fall models (e.g. Schneider et al. 2016), but a free-fall model is unlikely since the infall velocities of the observed clumps are lower than the free-fall value (e.g. Wyrowski et al. 2016).

If we ignore magnetic fields and bulk motions of the gas, the virial mass of a source can be estimated with the formula (MacLaren et al. 1988; Evans 1999):

$$M_{\text{vir}} \approx 126 R_{\text{eff}} \Delta v_{\text{tur}}^2 (M_{\odot}), \quad (3)$$

where R_{eff} is the source effective radius in pc, and Δv_{tur} is the turbulent line width in km s^{-1} (see also NH_3 (1, 1) velocity dispersion in Figure 5),

$$\Delta v_{\text{tur}}^2 = \Delta v_{\text{NH}_3(1,1)}^2 - \Delta v_{\text{ther}}^2 = \Delta v_{\text{NH}_3(1,1)}^2 - \frac{8 \ln(2) k T_{\text{kin}}}{m_{\text{NH}_3(1,1)}}, \quad (4)$$

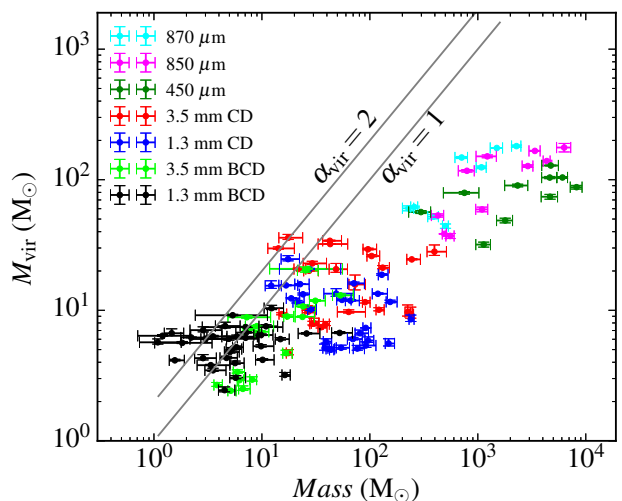


Fig. 6. Virial mass-dust mass distributions of all sources at different wavelengths. The two straight grey lines show thresholds of virial parameters $\alpha_{\text{vir}} = 1$ and $\alpha_{\text{vir}} = 2$.

where k is the Boltzmann constant and $m_{\text{NH}_3(1,1)}$ is the mass of the ammonia molecule. The corresponding data are listed in Tables D.1, D.2, and D.3. For the condensations in the 1.3 mm BCD configuration observations, the adopted line widths are estimated using the NH_3 (1, 1) line observations, which have a synthesized beam size of around 4 factor larger. There is no simple way of assigning NH_3 (1, 1) emission to each 1.3 mm fragment, as it is contaminated by emission from neighboring fragments. Some fragments have strong dynamical motions such as outflow and infall at a larger scale than our 1.3 mm beam. Therefore, the derived virial masses and virial parameters could be overestimated. The distribution between virial mass and dust mass is shown in Figure 6. We find that the clumps and cores at large scale are below the threshold with $\alpha_{\text{vir}} < 1$, suggesting that they are gravitationally bound, while a few part of the condensations at small scale are above the threshold with $\alpha_{\text{vir}} > 1$, indicating that they are gravitationally unbound and may be dispersing. This suggests that some of the condensations are unable to form stars. If we adopt $\alpha_{\text{vir}} = 2$ as a threshold for the critical virial parameter of a hydrostatic equilibrium sphere (Kauffmann et al. 2013), most clumps and fragments are gravitationally bound. This is consistent with the conclusion we arrived at by studying the radial density profile.

5.3. Fragmentation

Jeans fragmentation tends to produce numerous small fragments rather than a single massive object. The thermal Jeans mass M_J depends on gas temperature T and gas number density n as $M_J = 6.285 T^{1.5} n^{-0.5}$ (Palau et al. 2013). For a fragment at a gas temperature of 18 K and gas number density of 10^6 cm^{-3} , the thermal Jeans mass is $\sim 0.5 M_{\odot}$. The measured masses in Tables D.2 and D.3 are much larger than the value of $0.5 M_{\odot}$ suggesting that the fragments are gravitationally unstable. Other physical ingredients, such as radiation feedback, magnetic fields, turbulence and dynamic processes could play a role in forming cores above the thermal Jeans mass, thereby influencing the cloud fragmentation properties (refer to a review by Tan et al. 2014).

At larger scales with the lower resolution at $870 \mu\text{m}$, each clump shows just one or two relatively compact components.

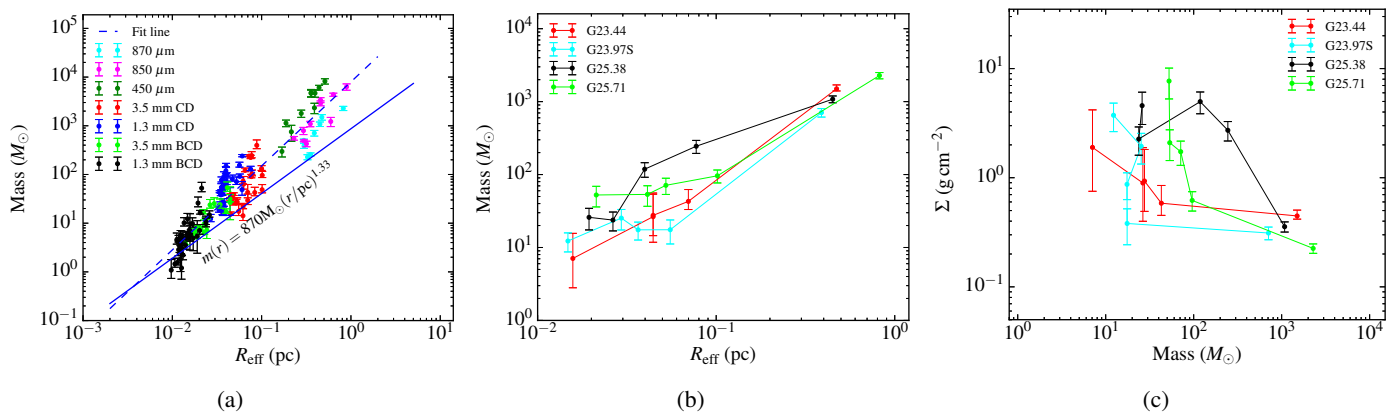


Fig. 7. (a) *Mass-size* distribution of all sources at different wavelengths, (b) *mass-size* and (c) *surface density-mass* distributions only for the most massive objects within each clump. The straight line shows the empirical threshold for high-mass star formation (Kauffmann & Pillai 2010). The dashed line shows the result of a linear power-law fit to the whole sample: $\log(\text{Mass}(R_{\text{eff}})/M_{\odot}) = 3.86 + 1.68 \times \log(R_{\text{eff}}/\text{pc})$ (see details in Zhang & Li 2017).

The masses of the eight clumps range from 228 to 2279 M_{\odot} , which provides sufficient material for the formation of stellar clusters (Blitz 1991; Blitz & Williams 1999). We find that towards the two lowest mass and lowest surface density clumps ($\Sigma = 0.14 \text{ g cm}^{-2}$), no compact sources are found, and we exclude the presence of compact fragments at our sensitivity limit of around $10 M_{\odot}$. The lowest surface density where we start to see compact sources is $\Sigma > 0.23 \text{ g cm}^{-2}$. In comparison, the study of Csengeri et al. (2017) identifies massive clumps with $\Sigma > 0.5 \text{ g cm}^{-2}$ as potential high-mass protostellar candidates.

We find that the brightest fragments within the infrared bright clumps are always associated with compact 1.3 cm radio emission. The observed radio emission is likely associated with the deeply embedded UC H II regions. Altogether we identify four clumps (G23.44-1, G23.97S-1, G25.71-1, and G25.71-2 at $850 \mu\text{m}$) as hosting compact H II regions. In general, these clumps have a rather low number of fragments up to spatial scales of $\sim 3\text{--}4''$. All of these fragments are associated with deeply embedded mid-infrared point sources. This picture is, however, somewhat different for the infrared quiet clumps. Two out of the four have no compact sources, and the other two sources, G18.17 and G18.21, only show weak $24 \mu\text{m}$ point sources towards the position of the fragments. From the low temperature estimates given by the NH_3 inversion transitions, these cores are likely to be cold, and thus potentially in an early phase of star formation. The core masses range up to $35 M_{\odot}$ suggesting that they already harbour sufficient mass to form at least one B3–B0 type star assuming 20–40% efficiency (Tanaka et al. 2016).

5.4. Mass-size distributions

In Figure 7, we show the *mass-size* distribution for all and for only the most massive objects potentially forming high-mass stars in panel (a) and (b), respectively (see also other discussion in our previous work of Zhang & Li 2017). The panel (b) in Figure 7 shows that the fragmentation slope gradually flattens from large scale to small scale and from $870 \mu\text{m}$ to 1.3 mm, while the *surface density-mass* relation in the panel (c) gradually steepens. This indicates that as fragmentation size decrease, the fragment mass remains roughly constant while the surface density increases sharply. The central dense condensations at a scale of around 0.02 pc can contain most of the mass of the source

with little in the surrounding envelope. For the relatively young sources, e.g., G18.17 and G18.21, the mass does not concentrate on a single core, but instead in several cores with comparable masses (see also Figures D.1 and D.2). For the relatively evolved sources, e.g., G24.44, G23.97S, G25.38, and G25.71, however, the mass is concentrated in a single condensation (see also Figures 1, D.5, D.6, and D.7).

5.5. Evolutionary stages

Millimeter emission on scales of $>0.5 \text{ pc}$ is usually associated with near- and mid-infrared emission from embedded protostars. In this work, 870 , 850 , and $450 \mu\text{m}$ emission seems to correlate well with the infrared emission distribution morphologically, except for clumps G23.97N and G23.98. The strong infrared emission tracing a protostar is contained within a cold clump traced by the millimeter emission. The infrared-quiet cores could contain early protostars too faint to be detected in the IR at these distances.

The $24 \mu\text{m}$ emission can provide a hint of the evolutionary stage of star formation. Based on the $24 \mu\text{m}$ flux density, most of the sample are infrared quiet. In particular, three sources (G23.97N, G23.98, and G25.38-u) seem to be in the earliest phase, corresponding either to starless or prestellar clumps, because we find no indication for on-going star formation despite their considerable mass and surface density. In addition, there exist offsets between the condensations and infrared peaks. On the other hand, the brightest fragments that are associated with a mid-infrared point source are resolved multiple components at our highest resolution, most of which are difficult to associate with a $24 \mu\text{m}$ counterpart. This case is similar to the prestellar core with weak infrared emission near the protostar IRAS 16293 (Lis et al. 2016). Therefore, we suggest that some of the condensations will probably form a subsequent generation of high- and intermediate-mass stars.

Methanol masers (CH_3OH) are classified into two groups: Class I and Class II (Menten 1991). The latter typically coincide in position with hot molecular cores, compact H II regions, and near-IR sources (e.g. Minier et al. 2001; Ellingsen 2006; Fontani et al. 2010), which clearly gives an indication of their evolutionary status. Checking the 6-GHz methanol multi-beam maser (MMB) catalogue (Green et al. 2010; Breen et al. 2015), we find that three of our sources harbour class II methanol

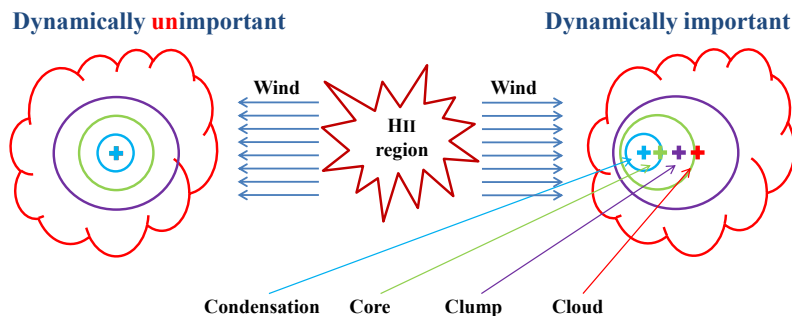


Fig. 8. A schematic illustration depicting the feedback of radiation from neighboring UC H II regions onto molecular clouds. The feedback could induce a position offset of centroid for the embedded clumps, cores, and condensations. The pluses “+” in different colors indicate corresponding position center of each object.

masers: G23.44, G23.97S, and G25.71 (see Figures 1, D.5, and D.7, respectively), which are all associated with 1.3 cm continuum emission. The Class II masers are located at the peak positions of the most massive condensations in clusters. It seems that the Class II methanol maser sources are the ones associated with free-free emission. The association with radio free-free emission is an indicator of a deeply embedded UC H II region, suggesting that that fragment has already a high-mass star with ionising radiation. Therefore, the sources G23.44, G23.97S, and G25.71 may be at the compact H II region stage, but are enveloped in a thick and cold dust envelope.

It is possible that a triggered hierarchical evolutionary sequence may exist, starting with the UC H II regions and following an early star-forming dense cores and condensations. In the following section, we will look for evidence of triggered star formation.

5.6. Triggered star formation by neighboring H II regions?

Whether, and to what extent, star formation is influenced by triggering remains an open question. Young star-forming regions are often surrounded by evolved OB stars or UC H II regions (Zhang et al. 2017b). In this study, all sources are close to one or two H II regions, which have already evolved into an advanced stage. The uniqueness of the sample enables us to study the effect of triggering on the dynamical evolution of gas clumps. The idea is to study the effect of the H II region on the internal dynamics of the clumps. If the expansion of the H II region is dynamically important, we expect it to have a noticeable effect on the morphology of the clumps. For example, the density structures of the clump would become spatially asymmetric (e.g., when the high density regions reside close to the trigger source), such that the most massive objects at different scales would align in line directed towards nearby H II regions (see a schematic illustration in Figure 8). If triggering is dynamically unimportant, we expect to structures at different scales (and thus different densities) to form either spherically-symmetric structure or with a random distribution of asymmetries.

To quantify the spatial asymmetry in the observations, Figure 9 displays the position offset⁷ for the most massive objects

⁷ In Figure 9, the pointing accuracy for the LABOCA and SCUBA-2 was, respectively, $\sim 4''$ (Schuller et al. 2009) and $1.5\text{--}2''$ (see <https://stfc.ukri.org/files/jcmtprospectuspdf/>). The position accuracy in a radio interferometric observation is of the order of 1/10th–1/20th of the synthesized beam (see https://www.iram.fr/IRAMFR/IS/IS2002/html_2/node130.html).

derived from observations at each spatial scale. We find that the sources G23.97N, G23.97S, and G23.44 show asymmetric spatial features with high density regions that do not reside at the center of the region and fragmented cores align in a string (see Figure 9), indicating that the strong stellar wind from the nearby H II region has affected on the thick clump envelope. In contrast, G25.71 shows a spherically symmetric feature, suggesting that after clump formation, the internal dynamics is self-regulated and independent of outside environment. This is consistent with the picture proposed by Li (2017) that the clump belongs to a regime where the collapse is self-regulated and is dynamically detached from the background fluid. Therefore, our findings imply that although the collapse is self-regulated, external triggering might still be able to create an asymmetric initial condition that might affect further fragmentation. We also note that the current sample is still not large enough, and we expect to be able to constrain this better using this method with a larger dataset. Furthermore, a random numerical simulation will be carried out in a forthcoming work.

6. Summary

We present multi-wavelength continuum observations towards a sample (G18.17, G18.21, G23.97N, G23.98, G23.44, G23.97S, G25.38, and G25.71) of high-mass star-forming clumps using radio- and millimeter interferometric data with arcsec resolution taken at 1.3 cm, 3.5 mm, 1.3 mm, and $870\ \mu\text{m}$. Our sample is unique as all the clumps are close to H II regions. This enables us to understand the effect of an external H II region on gravitational collapse.

We find that the targeted clumps have a mass range of 228 to $2279 M_{\odot}$ with $R_{\text{eff}} \sim 0.5\ \text{pc}$ and $n_{\text{H}_2} \sim 10^5\ \text{cm}^{-3}$. The brightest continuum sources are associated with infrared bright clumps and radio continuum sources. Two of the infrared quiet clumps host compact sources with masses up to $\sim 35 M_{\odot}$ and are capable of forming B3-B0 type stars. Two infrared quiet clumps with low surface densities ($\Sigma \sim 0.14\ \text{g cm}^{-2}$) show no compact fragments at 3.5 mm, indicating that star formation may not have yet started and might not occur in the future. Three sources (G23.97N, G23.98, and G25.38-u) show no indication of star formation despite their considerable mass and surface density and are starless, possibly prestellar clumps. The sources G23.44, G23.97S, and G25.71 may host ultra-compact H II regions, but they are deeply embedded in a thick and cold dust envelope.

The *mass – size* relation shows that the fragmentation slope gradually flattens from large scale to small scale and from $870\ \mu\text{m}$ to 1.3 mm, while the *surface density-mass* relation grad-

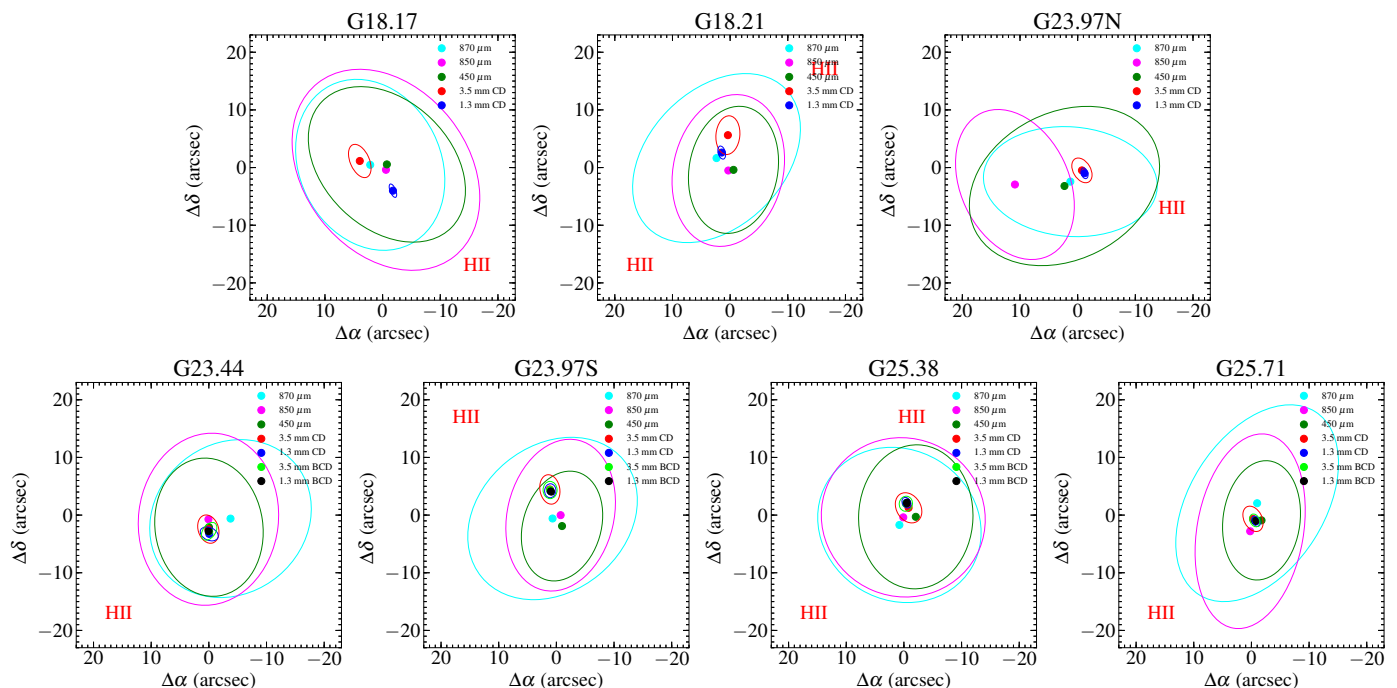


Fig. 9. The distribution of position offset for the most massive objects (in different color points with associated ellipse) derived from different scale observations. The ellipse shows the Gaussian size of each object. The text “H II” presents the location and direction of nearby H II regions. The offset (0, 0) is the phase center of the observations.

ually steepens. This indicates that as fragmentation size decrease, the fragment mass remains roughly constant while the surface density increases sharply. The central dense condensations at a scale of around 0.02 pc can contain most of the mass of the source with little in the surrounding envelope.

Taking advantage of the fact that all clumps have neighboring H II regions, we test triggered star formation using a novel method where we study the alignment of the centres of mass traced by dust emission at multiple scales with the position of external H II regions. If triggering is dynamically important, we expect the gas in the clump to be spatially aligned to due to external compression. Our investigations yield no clear patterns, which imply that collapse is self-regulated (regulated by the process of gravitational collapse) and the effect of external triggering is minimized after gravitational collapsed has begun. However, this needs to be confirmed by future studies with larger samples and a random numerical simulation.

Acknowledgements

We thank the anonymous referee for prompting many clarifications of this paper. This work is supported by the National Natural Science Foundation of China 11703040 and National Key Basic Research Program of China (973 Program) 2015CB857101. C.-P. Zhang acknowledges support by the MPG-CAS Joint Doctoral Promotion Program (DPP) and China Scholarship Council (CSC) in Germany as a postdoctoral researcher. T. Csengeri and T. Pillai acknowledge support from the *Deutsche Forschungsgemeinschaft*, DFG via the SPP (priority programme) 1573 ‘Physics of the ISM’.

References

Ai, M., Zhu, M., Xiao, L., & Su, H.-Q. 2013, *Research in Astronomy and Astrophysics*, 13, 935

- Anderson, L. D. & Bania, T. M. 2009, *ApJ*, 690, 706
- Ballesteros-Paredes, J., Hartmann, L. W., Vázquez-Semadeni, E., Heitsch, F., & Zamora-Avilés, M. A. 2011, *MNRAS*, 411, 65
- Battersby, C., Bally, J., Ginsburg, A., et al. 2011, *A&A*, 535, A128
- Benjamin, R. A., Churchwell, E., Babler, B. L., et al. 2003, *PASP*, 115, 953
- Beuther, H., Linz, H., Tackenberg, J., et al. 2013, *A&A*, 553, A115
- Blitz, L. 1991, in *NATO Advanced Science Institutes (ASI) Series C*, Vol. 342, NATO Advanced Science Institutes (ASI) Series C, ed. C. J. Lada & N. D. Kylafis, 3
- Blitz, L. & Williams, J. P. 1999, in *NATO Advanced Science Institutes (ASI) Series C*, Vol. 540, NATO Advanced Science Institutes (ASI) Series C, ed. C. J. Lada & N. D. Kylafis, 3
- Bonnell, I. A. & Bate, M. R. 2002, *MNRAS*, 336, 659
- Bonnell, I. A., Bate, M. R., Clarke, C. J., & Pringle, J. E. 2001, *MNRAS*, 323, 785
- Bonnell, I. A., Vine, S. G., & Bate, M. R. 2004, *MNRAS*, 349, 735
- Breen, S. L., Fuller, G. A., Caswell, J. L., et al. 2015, *MNRAS*, 450, 4109
- Brunthaler, A., Reid, M. J., Menten, K. M., et al. 2009, *ApJ*, 693, 424
- Carey, S. J., Noriega-Crespo, A., Mizuno, D. R., et al. 2009, *PASP*, 121, 76
- Churchwell, E. 2002, *ARA&A*, 40, 27
- Churchwell, E., Babler, B. L., Meade, M. R., et al. 2009, *PASP*, 121, 213
- Csengeri, T., Bontemps, S., Schneider, N., Motte, F., & Dib, S. 2011a, *A&A*, 527, A135
- Csengeri, T., Bontemps, S., Schneider, N., et al. 2011b, *ApJ*, 740, L5
- Csengeri, T., Bontemps, S., Wyrowski, F., et al. 2017, *A&A*, 600, L10
- Csengeri, T., Urquhart, J. S., Schuller, F., et al. 2014, *A&A*, 565, A75
- Dale, J. E., Bonnell, I. A., & Whitworth, A. P. 2007, *MNRAS*, 375, 1291
- Donkov, S. & Stefanov, I. Z. 2018, *MNRAS*, 474, 5588
- Ellingsen, S. P. 2006, *ApJ*, 638, 241
- Elmegreen, B. G. 2011, in *EAS Publications Series*, Vol. 51, EAS Publications Series, ed. C. Charbonnel & T. Montmerle, 45–58
- Evans, II, N. J. 1999, *ARA&A*, 37, 311
- Fontani, F., Cesaroni, R., & Furuya, R. S. 2010, *A&A*, 517, A56
- Galván-Madrid, R., Keto, E., Zhang, Q., et al. 2009, *ApJ*, 706, 1036
- Girichidis, P., Konstantin, L., Whitworth, A. P., & Klessen, R. S. 2014, *ApJ*, 781, 91
- Green, J. A., Caswell, J. L., Fuller, G. A., et al. 2010, *MNRAS*, 409, 913
- Gutermuth, R. A. & Heyer, M. 2015, *AJ*, 149, 64
- Henney, W. J., Arthur, S. J., de Colle, F., & Mellema, G. 2009, *MNRAS*, 398, 157
- Ho, P. T. P. & Townes, C. H. 1983, *ARA&A*, 21, 239
- Kauffmann, J., Bertoldi, F., Bourke, T. L., Evans, II, N. J., & Lee, C. W. 2008, *A&A*, 487, 993
- Kauffmann, J. & Pillai, T. 2010, *ApJ*, 723, L7

Kauffmann, J., Pillai, T., & Goldsmith, P. F. 2013, *ApJ*, 779, 185
 Klein, R. I., Sandford, II, M. T., & Whitaker, R. W. 1980, *Space Sci. Rev.*, 27, 275
 Klessen, R. S. & Burkert, A. 2001, *ApJ*, 549, 386
 Kramer, C., Stutzki, J., Rohrig, R., & Corneliussen, U. 1998, *A&A*, 329, 249
 Larson, R. B. 1969, *MNRAS*, 145, 271
 Li, G.-X. 2017, *MNRAS*, 465, 667
 Li, G.-X. 2018, *MNRAS*, 477, 4951
 Lis, D. C., Wootten, H. A., Gerin, M., et al. 2016, *ApJ*, 827, 133
 Lockman, F. J. 1989, *ApJS*, 71, 469
 MacLaren, I., Richardson, K. M., & Wolfendale, A. W. 1988, *ApJ*, 333, 821
 Makovoz, D. & Marleau, F. R. 2005, *PASP*, 117, 1113
 Marton, G., Calzoletti, L., Perez Garcia, A. M., et al. 2017, *ArXiv e-prints*: 1705.05693
 McKee, C. F. & Tan, J. C. 2002, *Nature*, 416, 59
 McKee, C. F. & Tan, J. C. 2003, *ApJ*, 585, 850
 Menten, K. M. 1991, *ApJ*, 380, L75
 Mezger, P. G. & Henderson, A. P. 1967, *ApJ*, 147, 471
 Minier, V., Conway, J. E., & Booth, R. S. 2001, *A&A*, 369, 278
 Molinari, S., Schisano, E., Elia, D., et al. 2016, *A&A*, 591, A149
 Motte, F., Bontemps, S., & Louvet, F. 2018, *ARA&A*, 56, 41
 Motte, F., Bontemps, S., Schilke, P., et al. 2007, *A&A*, 476, 1243
 Murray, N. & Chang, P. 2015, *ApJ*, 804, 44
 Myers, P. C. 1998, *ApJ*, 496, L109
 Naranjo-Romero, R., Vázquez-Semadeni, E., & Loughnane, R. M. 2015, *ApJ*, 814, 48
 Ossenkopf, V. & Henning, T. 1994, *A&A*, 291, 943
 Ott, J., Henkel, C., Braatz, J. A., & Weiß, A. 2011, *ApJ*, 742, 95
 Padoan, P. & Nordlund, Å. 2002, *ApJ*, 576, 870
 Palau, A., Fuente, A., Girart, J. M., et al. 2013, *ApJ*, 762, 120
 Penston, M. V. 1969, *MNRAS*, 144, 425
 Pillai, T., Kauffmann, J., Wyrowski, F., et al. 2011, *A&A*, 530, A118
 Pillai, T., Wyrowski, F., Hatchell, J., Gibb, A. G., & Thompson, M. A. 2007, *A&A*, 467, 207
 Planck Collaboration, Ade, P. A. R., Aghanim, N., et al. 2014, *A&A*, 564, A45
 Poglitsch, A., Waelkens, C., Geis, N., et al. 2010, *A&A*, 518, L2
 Pokhrel, R., Myers, P. C., Dunham, M. M., et al. 2018, *ApJ*, 853, 5
 Reid, M. J., Menten, K. M., Zheng, X. W., et al. 2009, *ApJ*, 700, 137
 Russeil, D., Zavagno, A., Motte, F., et al. 2010, *A&A*, 515, A55
 Sandford, II, M. T., Whitaker, R. W., & Klein, R. I. 1982, *ApJ*, 260, 183
 Schneider, N., Bontemps, S., Motte, F., et al. 2016, *A&A*, 587, A74
 Schneider, N., Csengeri, T., Bontemps, S., et al. 2010, *A&A*, 520, A49
 Schuller, F., Menten, K. M., Contreras, Y., et al. 2009, *A&A*, 504, 415
 Shu, F. H. 1977, *ApJ*, 214, 488
 Stutzki, J. & Guesten, R. 1990, *ApJ*, 356, 513
 Sugitani, K., Fukui, Y., Mizuni, A., & Ohashi, N. 1989, *ApJ*, 342, L87
 Tan, J. C., Beltrán, M. T., Caselli, P., et al. 2014, *Protostars and Planets VI*, 149
 Tanaka, K. E. I., Tan, J. C., & Zhang, Y. 2016, *ApJ*, 818, 52
 Thompson, M. A., Gibb, A. G., Hatchell, J. H., Wyrowski, F., & Pillai, T. 2005, in *ESA Special Publication, Vol. 577, ESA Special Publication*, ed. A. Wilson, 425–426
 Urquhart, J. S., Moore, T. J. T., Csengeri, T., et al. 2014, *MNRAS*, 443, 1555
 Urquhart, J. S., Thompson, M. A., Moore, T. J. T., et al. 2013, *MNRAS*, 435, 400
 Vázquez-Semadeni, E., Gómez, G. C., Jappsen, A.-K., Ballesteros-Paredes, J., & Klessen, R. S. 2009, *ApJ*, 707, 1023
 Wang, K., Zhang, Q., Testi, L., et al. 2014, *MNRAS*, 439, 3275
 Wang, K., Zhang, Q., Wu, Y., & Zhang, H. 2011, *ApJ*, 735, 64
 Whitworth, A. P., Bhattal, A. S., Chapman, S. J., Disney, M. J., & Turner, J. A. 1994, *MNRAS*, 268, 291
 Wienen, M., Wyrowski, F., Schuller, F., et al. 2012, *A&A*, 544, A146
 Williams, J. P., Blitz, L., & McKee, C. F. 2000, *Protostars and Planets IV*, 97
 Woody, D. P., Scott, S. L., Scoville, N. Z., et al. 1989, *ApJ*, 337, L41
 Wyrowski, F., Güsten, R., Menten, K. M., et al. 2016, *A&A*, 585, A149
 Zhang, C.-P. & Li, G.-X. 2017, *MNRAS*, 469, 2286
 Zhang, C.-P., Li, G.-X., Wyrowski, F., et al. 2016, *A&A*, 585, A117
 Zhang, C. P. & Wang, J. J. 2012, *A&A*, 544, A11
 Zhang, C.-P., Wang, J.-J., & Xu, J.-L. 2013, *A&A*, 550, A117
 Zhang, C.-P., Wang, J.-J., Xu, J.-L., Wyrowski, F., & Menten, K. M. 2014, *ApJ*, 784, 107
 Zhang, C.-P., Yuan, J.-H., Li, G.-X., Zhou, J.-J., & Wang, J.-J. 2017a, *A&A*, 598, A76
 Zhang, C.-P., Yuan, J.-H., Xu, J.-L., et al. 2017b, *Research in Astronomy and Astrophysics*, 17, 057
 Zhang, Q., Wang, Y., Pillai, T., & Rathborne, J. 2009, *ApJ*, 696, 268

Appendix A: Distinguishing the ionised gas from cold dust

Towards compact H II regions, the measured continuum fluxes near 3.5 mm have contributions from both the ionised gas and dust emission (Churchwell 2002; Zhang et al. 2014). The free-free emission from ionised gas may strongly boost the flux at 3.5 mm, when a bright H II region or protostar is located in the field. For the mass estimations based on the dust, it is, therefore, necessary to distinguish between the contaminating free-free emission and the thermal dust emission. In this work, we used archival continuum data at 6 cm and 1.3 cm to look for point sources associated with the dust peaks. The 6 cm data is from the Co-Ordinated Radio ‘N’ Infrared Survey for High-mass star formation (CORNISH), which has a spatial resolution of 1.5'' with a noise level <0.4 mJy beam $^{-1}$. The 1.3 cm continuum is derived from our VLA observations (see Section 2.4) with a noise level of 0.6–1.2 mJy beam $^{-1}$. If the 6 cm or 1.3 cm emission cannot be detected above 3σ , we use the 3σ upper limit for the fitting of their spectral energy distribution (SED). Towards 27 dust cores, we detect 4 sources (G23.44-1, G23.97S-1, G25.71-1, and G25.71-2) with free-free emission judging from the 1.3 cm data (see Figure 1), while only the sources G25.71-1 and G25.71-2 have 6 cm emission. These detections are consistent with these clumps being classified as infrared bright clumps. We estimate the contamination by free-free emission using SED fitting combining 6 cm (CORNISH), 1.3 cm (VLA), 3.5 mm (PdBI), 1.3 mm (PdBI), 870 μ m (ATLASGAL), 850 μ m (SCUBA), and 450 μ m (SCUBA).

For SED fitting (see also Figure A.1), the free-free emission model (Mezger & Henderson 1967) is

$$\begin{cases} S_\nu = \Omega_s B_\nu(T_e)(1 - e^{-\tau_c})(\text{Jy}) \\ \tau_c = 0.08235 \alpha(\nu, T_e) \left(\frac{\nu}{\text{GHz}}\right)^{-2.1} \left(\frac{T_e}{\text{K}}\right)^{-1.35} \left(\frac{EM}{\text{pc cm}^{-6}}\right), \end{cases} \quad (\text{A.1})$$

where S_ν is the integration flux at frequency ν , Ω_s is the solid angle, $B_\nu(T_e)$ is the Planck function with variable electron temperature T_e , $\alpha(\nu, T_e) \sim 1$, and EM is the emission measure. The dust emission enters (Woody et al. 1989) as

$$\left(\frac{S_\nu}{\text{Jy}}\right) = 52.36 \left(\frac{M}{M_\odot}\right) \left(\frac{0.25}{\lambda_{\text{mm}}}\right)^{\beta+3} \left[e^{\left(\frac{14.4}{\lambda_{\text{mm}} T_{\text{dust}}}\right)} - 1\right]^{-1} \left(\frac{D}{\text{kpc}}\right)^{-2}, \quad (\text{A.2})$$

where M is the mass of dusty gas, β is the spectral index of the dust emissivity, T_{dust} is the dust temperature (approximately equal to kinetic temperature; see Section A) in Kelvin, λ_{mm} is the wavelength in mm, and D is the distance. In the models, we let M , T_e , and EM vary as free parameters, set β to 1.7 (Battersby et al. 2011; Planck Collaboration et al. 2014), and use the least square method to fit the data. For the 6 cm data, we use its 3σ upper limit; for other wavelength data, we use `Gaussclumps` to extract their fluxes as listed in Tables D.1, D.2, and D.3. The 870, 850, and 450 μ m data are from single dish observations and have much lower resolutions than other interferometer data in this work. However, the single dish observations can be used to measure total flux of each source. To estimate missing masses at different scales between interferometer and single dish observations, the wavelengths at 870, 850, and 450 μ m don't participate in the SED fitting. Additionally, we assume that the turnover occurs shortward of 3.5 mm at wavelengths where the free-free is already negligible compared to the dust emission.

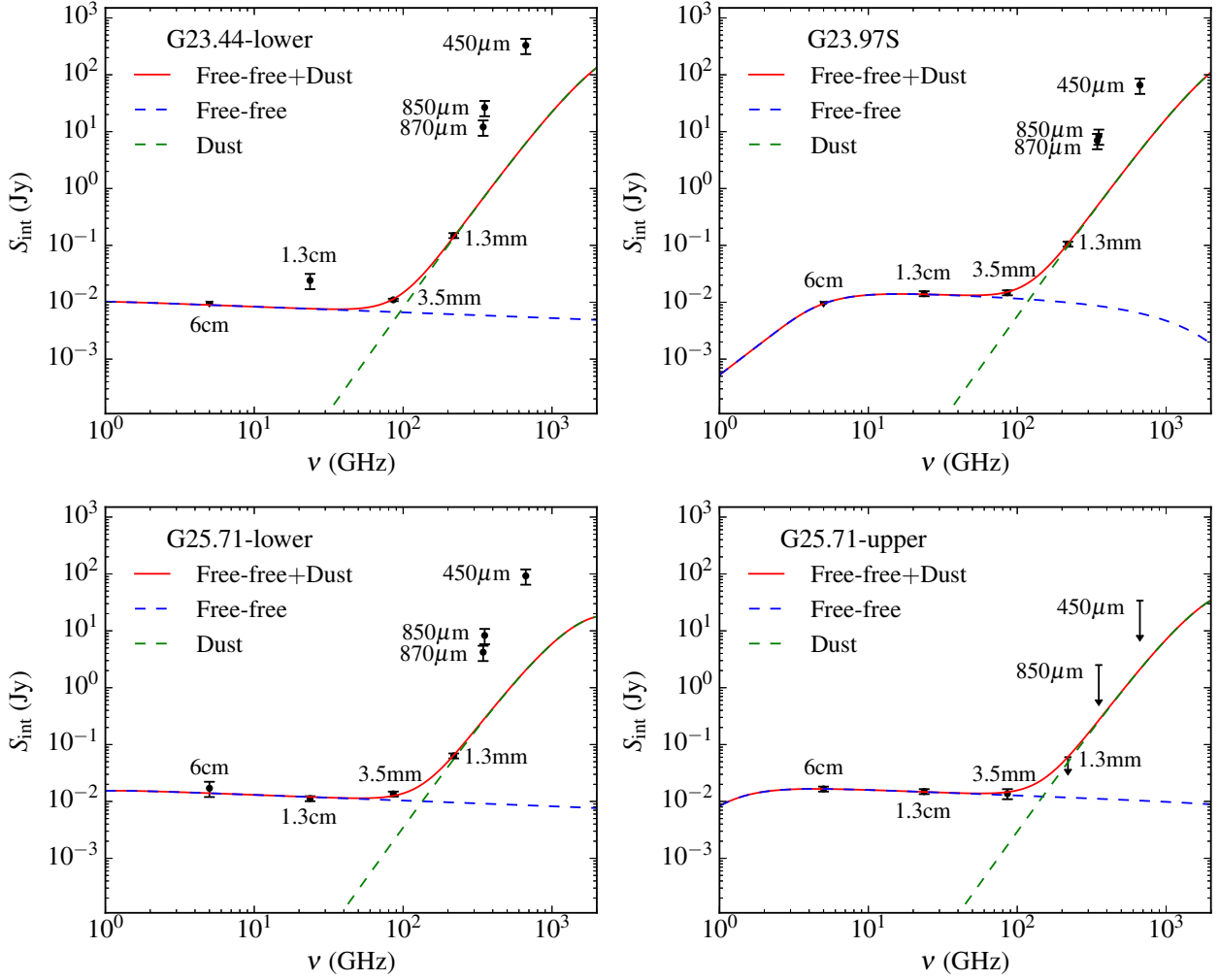


Fig. A.1. SED fittings for cores G23.44-l, G23.97S, G25.71-l, and G25.71-u, combining 6 cm (CORNISH), 1.3 cm (VLA), 3.5 mm (PdBI), 1.3 mm (PdBI), 870 μm (ATLASGAL), 850 μm (SCUBA), and 450 μm (SCUBA). The spectral index of the dust emissivity is set as $\beta = 1.7$. The ionised gas and cold dust components were shown in dashed blue and dashed green lines, respectively. For core G25.71-u, there is no observation at 1.3 mm for its offset away from the primary beam size, so we take the measurements on 850 and 450 μm flux as two upper limits.

From the SED fitting, we find that the contribution from the dust emission to the measured total continuum flux is significant, e.g., 40.8% for G23.44 (No.1 for CD and BCD configuration observations) and 21.7% for G23.97S (No.1 for CD and BCD configuration observations) at 3.5 mm. These results are indicated in Table D.2. The 1.3 mm flux is also a key parameter in distinguishing the dust component from free-free emission with SED fitting. If the cores are not detected at 6 cm and 1.3 cm emission, we will assume that the contribution is 100% from dust emission.

Appendix B: Missing flux

Interferometric observations filter out emission from large scales due to missing information on short spacings for the 1.3 mm observations. According to the interferometer baseline range of 16.0 m (11.7 $k\lambda$) to 452.1 m (331.1 $k\lambda$), we obtain a rough estimate of about 21.6'' above which flux is filtered out. This means that we recover emission from the compact sources only up to these scales, which impacts the mass estimates. As Figure A.1 shows, the fitted fluxes at 870 μm are much lower than the measured fluxes. The difference between the measured and fitted fluxes at 870 μm suggests that between 92.0% to 94.6% of the flux is filtered out by the interferometer. Assuming that the gas

emitting and 1.3 mm and at 870 μm has the same origin, we can extrapolate that typically a large fraction of the flux at 1.3 mm is lost by filtering from the clump to the condensation scale. We find two clumps where all the flux seems to be filtered by the interferometer suggesting that there are no bright compact objects formed yet within these clumps.

In practice, the high resolution interferometric observations typically resolve the clumps into several fragments. We derived their masses based on our SED fitting with which we disentangled contribution of the thermal dust and the free-free emission, and therefore could estimate the mass of each fragment on 5000 AU size scales. If we take into account that the 870 μm flux is not entirely emitted from the same region as the 1.3 mm condensation, to more accurately derive missing flux we should estimate the mass ratio between the most massive condensation and the clustered condensations of each clump. In the 1.3 mm CD configuration observations, the most massive condensation within each cluster takes between 40.6% and 66.3% of the total condensation mass, which means that about 50% of the clump mass had been resolved out into other fragments at higher resolutions. Based on above, there may exist about 46.0% (50% \times 92.0%) to 47.3% (50% \times 94.6%) missing flux above a typical scale of 21.6'', due to missing short spacings.

Appendix C: Individual clumps

Appendix C.1: G18.17

This clump is infrared quiet with flux $S_{24\mu\text{m}} = 214.9$ mJy at $24\mu\text{m}$ (see Table 3), and has a neighboring UC H II region (see Figure D.1(a) and also the work in Zhang et al. 2017b). It is located at a near kinematic distance of 3.73 kpc (Wienen et al. 2012; Reid et al. 2009). Given the strong infrared bright background, it is difficult to present our relatively weak target in Figure D.1(a). At $8.0\mu\text{m}$ there is one apparently bow-shaped border separating the clump G18.17 from the UC H II region, indicating radiation feedback from the UC H II region nearby (Zhang et al. 2017b). At $70\mu\text{m}$, both of them are probably merging together, but we can still identify the clump G18.17 with a convex morphology.

There is no detected emission at 6 and 1.3 cm (see Figure D.1(c)), so G18.17 is not a candidate UC H II region. There is strong dust emission at 870, 850, and $450\mu\text{m}$, which is highly consistent with the weak $70\mu\text{m}$ emission. The derived mass is about $387.3 M_{\odot}$ with an effective radius $R_{\text{eff}} = 0.30$ pc at $870\mu\text{m}$. From the physical parameters, we believe that the clump G18.17 is a very early high-mass star-forming candidate. This clump has fragmented into three cores each with a mass above $17.6 M_{\odot}$ at 3.5 mm, but there is almost no corresponding object at 1.3 mm above 5σ (see Figures D.1(d)(e)).

Appendix C.2: G18.21

From Figure D.2(a), the clump G18.21 has two bright UC H II regions nearby (see also the work in Zhang et al. 2017b). The photometric flux of the clump at $24\mu\text{m}$ is 773.3 mJy, and belongs to infrared quiet source (see Table 3). The emission at $70\mu\text{m}$ is very weak at only 4.6 Jy. It is located at a near kinematic distance of 3.60 kpc (Wienen et al. 2012; Reid et al. 2009). The clump G18.21 is embedded in an infrared dark cloud. There is no detected emission at 6 or 1.3 cm. The bright emission at 870, 850, and $450\mu\text{m}$ shows that this clump is a cold and massive star-forming object with a mass of $501.8 M_{\odot}$ at $870\mu\text{m}$.

The clump has fragmented into two cores each with mass above $15.3 M_{\odot}$ ($R_{\text{eff}} = 0.045\text{--}0.052$ pc) at 3.5 mm. The condensation with a mass of $5.9 M_{\odot}$ ($R_{\text{eff}} = 0.016$ pc) identified at 1.3 mm is located at the middle position of the two cores at 3.5 mm. There is an obvious offset between the 3.5, 1.3 and $4.5\mu\text{m}$ peaks.

Appendix C.3: G23.97N

The clump G23.97N is in a similar condition to G18.17. It is located at a near kinematic distance of 4.68 kpc (Wienen et al. 2012; Reid et al. 2009). In Figure D.3(e), it is clear that the $4.5\mu\text{m}$ point source is located far away from the core position at 1.3 mm in Figure D.3(e), but is consistent with the positions of the 8.0 and $24\mu\text{m}$ point sources. The bright infrared point source nearby may be a background or foreground object corresponding to the clump G23.97N. Based on the above, we suggest that G23.97N, with very weak $70\mu\text{m}$ emission, may be a prestellar core.

There is no detected free-free emission in Figure D.3(c). The emission at 870, 850, and $450\mu\text{m}$ is very weak, relative to the other clumps in this work. The clump mass is $227.5 M_{\odot}$ ($R_{\text{eff}} = 0.33$ pc) at $870\mu\text{m}$; the core mass is $38.7 M_{\odot}$ ($R_{\text{eff}} = 0.049$ pc) at 3.5 mm, while the corresponding condensation mass is $8.1 M_{\odot}$ ($R_{\text{eff}} = 0.019$ pc) at 1.3 mm. Actually, we detect three

intermediate-mass condensations in a line above 5σ at 1.3 mm. Their distributions are correlative to the filament structure at $850\mu\text{m}$ in Figure D.3(b).

Appendix C.4: G23.98

The clump G23.98 is infrared quiet with a $24\mu\text{m}$ flux of only 8.7 mJy and may be a prestellar core (Figure D.4). It is located at a near kinematic distance of 4.68 kpc (Wienen et al. 2012; Reid et al. 2009). Possibly due to contamination from the bright UC H II region nearby, it is difficult to show this weak source clearly at infrared wavelengths. This core may be optically thick condition or in a very early evolutionary stage.

The emission at 870, 850, and $450\mu\text{m}$ is also very weak. The mass is $258.1 M_{\odot}$ ($R_{\text{eff}} = 0.35$ pc) at $870\mu\text{m}$. There is no free-free emission at 6 or 1.3 cm, and no dust emission at 3.5 mm within its primary beam size. However, we detected only one condensation with a mass of $6.7 M_{\odot}$ ($R_{\text{eff}} = 0.018$ pc) at 1.3 mm, which is consistent with the clump G23.98 at $850\mu\text{m}$.

Appendix C.5: G23.44

The clump G23.44 has a trigonometric-parallax distance of 5.88 kpc (Brunthaler et al. 2009). In Figure 1(a), the three-color image shows one vague point source within 1.3 mm primary beam. The $70\mu\text{m}$ emission shows two adjacent clumps, designated lower (G23.44-l) and upper (G23.44-u), respectively. Their $24\mu\text{m}$ fluxes are 300.1 and 1683.5 mJy, respectively. The clumps G23.44-l and -u are thus classified into infrared bright and quiet sources, respectively. In Figure 1(c), we find that there is strong free-free emission (24.20 mJy beam $^{-1}$) with extended morphology at 1.3 cm for G23.44-l, but there is not any emission detected at 6 cm. The integrated flux at 3.5 mm is 11.01 mJy for core No.1 in Figure 1(d). The integrated flux at 1.3 cm is more than twice that at 3.5 mm, which means that the measured integrated flux at 3.5 mm is purely from free-free emission. That is very interesting and not convincing. We suggest that the derived integrated flux at 1.3 cm has a high uncertainty. We have to adopt an upper limit at 6 cm for SED fitting, in order to estimate the core mass at 3.5 mm (see Section A).

The emission at 870 and $850\mu\text{m}$ shows one very compact and bright clump. The mass is $1498.6 M_{\odot}$ ($R_{\text{eff}} = 0.47$ pc) at $870\mu\text{m}$. The emission at $450\mu\text{m}$ has two resolved components. In the 3.5 mm CD configuration observations in Figure 1(d), the clump fragments into 6 cores or two clusters (a lower cluster surrounding core No.1 and upper cluster surrounding core No.2). The two clusters are further resolved in the 3.5 mm BCD configuration observations in Figure 1(f). The masses of No.1 and No.2 are $27.6 M_{\odot}$ ($R_{\text{eff}} = 0.044$ pc) and $55.2 M_{\odot}$ ($R_{\text{eff}} = 0.038$ pc), respectively. In the 1.3 mm CD configuration observations in Figure 1(e), there are three massive and compact cores. In the 1.3 mm BCD configuration observations in Figure 1(g), there are 16 condensations in total. The most massive condensations No.1 and No.2 have a mass of $7.1 M_{\odot}$ ($R_{\text{eff}} = 0.016$ pc) and $5.6 M_{\odot}$ ($R_{\text{eff}} = 0.013$ pc), respectively. The upper clusters are close to the boundary of the primary beam at 1.3 mm, so their masses have large uncertainty.

Appendix C.6: G23.97S

The clump G23.97S is located at a near kinematic distance of 4.70 kpc (Wienen et al. 2012; Reid et al. 2009). In Figure D.5(a), there are two connected infrared point sources within the 1.3 mm

primary beam of the PdBI. Comparing with other wavelengths, we argue that the upper infrared source is associated with our target. The clump at infrared wavelengths is bright compared to the background. However, the 24 and 70 μm fluxes are just 709.6 mJy and 179.8 Jy. This source is therefore infrared quiet, but there is detectable free-free emission at 1.3 cm, so this source has a corresponding UC H II region.

This clump has strong emission at 870, 850, and 450 μm . The derived mass is 708.3 M_{\odot} within $R_{\text{eff}} = 0.39$ pc at 870 μm . In the 3.5 mm and 1.3 mm CD configuration observations (Figures D.5(d)(e)), we find that only the single core No.1 dominates the clusters. The core mass is 17.5 M_{\odot} with $R_{\text{eff}} = 0.055$ pc at 3.5 mm, and 25.3 M_{\odot} with $R_{\text{eff}} = 0.029$ pc at 1.3 mm. The clump fragments into a cluster of condensations with BCD configuration observations, especially in the 1.3 mm BCD configuration observations in Figure D.5(g). The most massive condensation No.1 is located in the south-west of the cluster. The condensation No.1 has a mass of 12.3 M_{\odot} with $R_{\text{eff}} = 0.015$ pc. The condensations No.2 and No.5 are intermediately massive (above 4.5 M_{\odot}).

Appendix C.7: G25.38

The clump G25.38 is located at a near kinematic distance of 5.60 kpc (Anderson & Bania 2009; Ai et al. 2013; Urquhart et al. 2013). In Figure D.6(a)(c), there is a very vague infrared point source within the 1.3 mm primary beam of the PdBI. At 3.5 mm, the clump G25.38 fragments into two clusters (Figure D.6(d)). In Table 3, the derived 24 μm fluxes are 252.3 mJy for G25.38-l, and no detection for G25.38-u, so they are infrared quiet sources. The infrared luminosity of G25.38-u has been contaminated by the extended UC H II region nearby. At 1.3 cm in Figure D.6(c), there is just extremely weak emission (about 3σ) located at the peak position of the infrared point source.

At 870, 850, and 450 μm , the clump shows a compact and bright structure. The clump mass is 1080.6 M_{\odot} with $R_{\text{eff}} = 0.45$ pc at 870 μm . The G25.38-u is located at the boundary of the 3.5 mm primary beam of the PdBI, which will introduce high noise. We believed that the G25.38-u is an independent clump, rather than a piece of the UC H II region nearby. However, it is likely that feedback from the UC H II region nearby has affected G25.38-u and G25.38-l. In Figure D.6(f), the clump has fragmented into 16 cores. The most massive object No.1 within 1.3 mm primary beam has a mass of 52.2 M_{\odot} with $R_{\text{eff}} = 0.040$ pc in the 3.5 mm BCD configuration observations. In Figure D.6(e), there are 4 cores in a filament morphology perpendicular to its parent clump (No.1, No.5, and No.8 are also in a filament structure, see Figure D.6(d)), which may be a dynamical effect. This case is similar to sources G28.34-P1 (Wang et al. 2011) and G11.11-P6 (Wang et al. 2014). They explained that it was due to cylindrical fragmentation. In Figure D.6(g), we can see one more compact structure than that in Figure D.6(e). The condensation No.1 has a mass of 25.9 M_{\odot} with $R_{\text{eff}} = 0.019$ pc in the 1.3 mm BCD configuration observations.

Appendix C.8: G25.71

The clump G25.71 is located at a near kinematic distance of 9.50 kpc (Urquhart et al. 2013; Lockman 1989). In Figure D.7(a), the extended UC H II region is located to the south-east of the clump G25.71. There are two fairly bright infrared point sources G25.71-l ($S_{24\mu\text{m}} = 6197.1$ mJy) and G25.71-u ($S_{24\mu\text{m}} = 16109.0$ mJy) within the 3.5 mm primary beam (see in Table 3). Based the criteria in Section 4.2, both the G25.71-l and G25.71-u

are infrared bright. The emission at 870, 850, and 450 μm shows an extended structure in a north-south direction. For the free-free emission at 1.3 cm, two compact points are well located at the peak positions of G25.71-u and G25.71-l, which are likely two compact H II region candidates.

In Figure D.7(d)(f), there are similar structures in the CD configuration observations and BCD configuration observations at 3.5 mm, but the core No.1 in the CD configuration observations fragments into three condensations in the BCD configuration observations. The mass of condensation No.1 is 71.2 M_{\odot} with $R_{\text{eff}} = 0.052$ pc in the 3.5 mm BCD configuration observations. In Figure D.7(e)(g), the cores show an elongated structure in an east-west direction, which may be from dynamical feedback or cylindrical fragmentation, similar to clump G25.38 (see analysis in Section C.7). The core No.1 in the 1.3 mm CD configuration observations fragmented into three condensations in the 1.3 mm BCD configuration observations. The mass of condensation No.1 is 52.5 M_{\odot} with $R_{\text{eff}} = 0.021$ pc in the 1.3 mm BCD configuration observations.

Appendix D: Other figures and tables

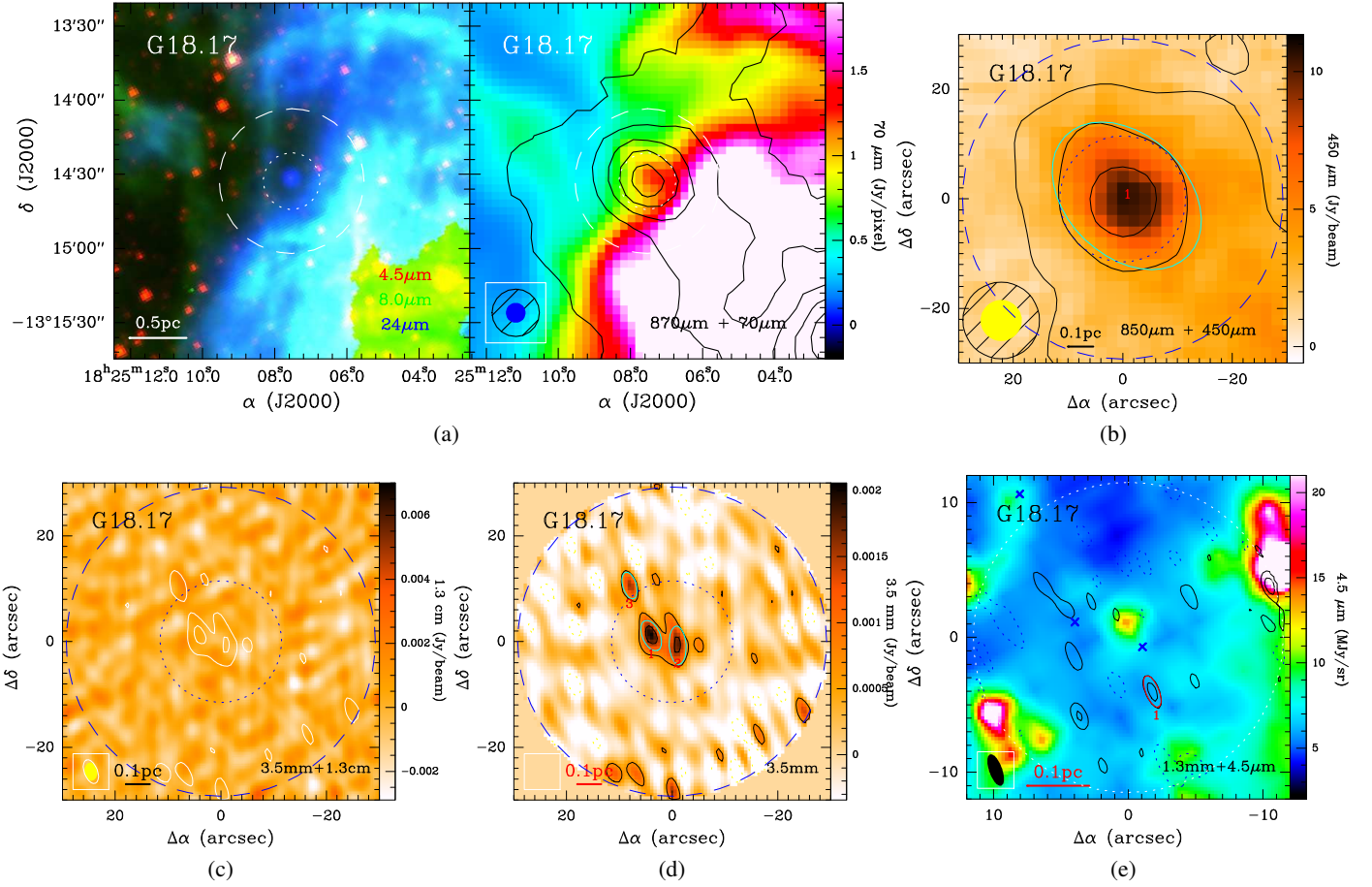


Fig. D.1. G18.17: (a) (left) Three-color image of 4.5 μm (blue), 8.0 μm (green), and 24 μm (red); (right) 870 μm contours overlaid on a 70 μm color scale. The 870 μm contour levels start at 6σ in steps of 8σ ($\sigma = 54 \text{ mJy beam}^{-1}$). (b) 850 μm contours overlaid on a 450 μm color scale. The 850 μm contour levels start at 6σ in steps of 8σ ($\sigma = 83 \text{ mJy beam}^{-1}$). (c) 3.5 mm contours overlaid on a 1.3 cm color scale. For CD configuration observations, (d) the 3.5 mm contour levels start at -3σ , 3σ in steps of 4σ ($\sigma = 0.23 \text{ mJy beam}^{-1}$), and (e) the 1.3 mm contour levels start at -3σ , 3σ in steps of 2σ ($\sigma = 1.67 \text{ mJy beam}^{-1}$) superimposed on a 24 μm color scale. The ellipses with numbers indicate the positions of extracted sources. The crosses in the 1.3 mm CD configuration observations indicate the positions of the corresponding 3.5 mm CD configuration observations. The dashed and dotted circles in each subfigure indicate the primary beam scales of 3.5 and 1.3 mm PdBI tracks, respectively.

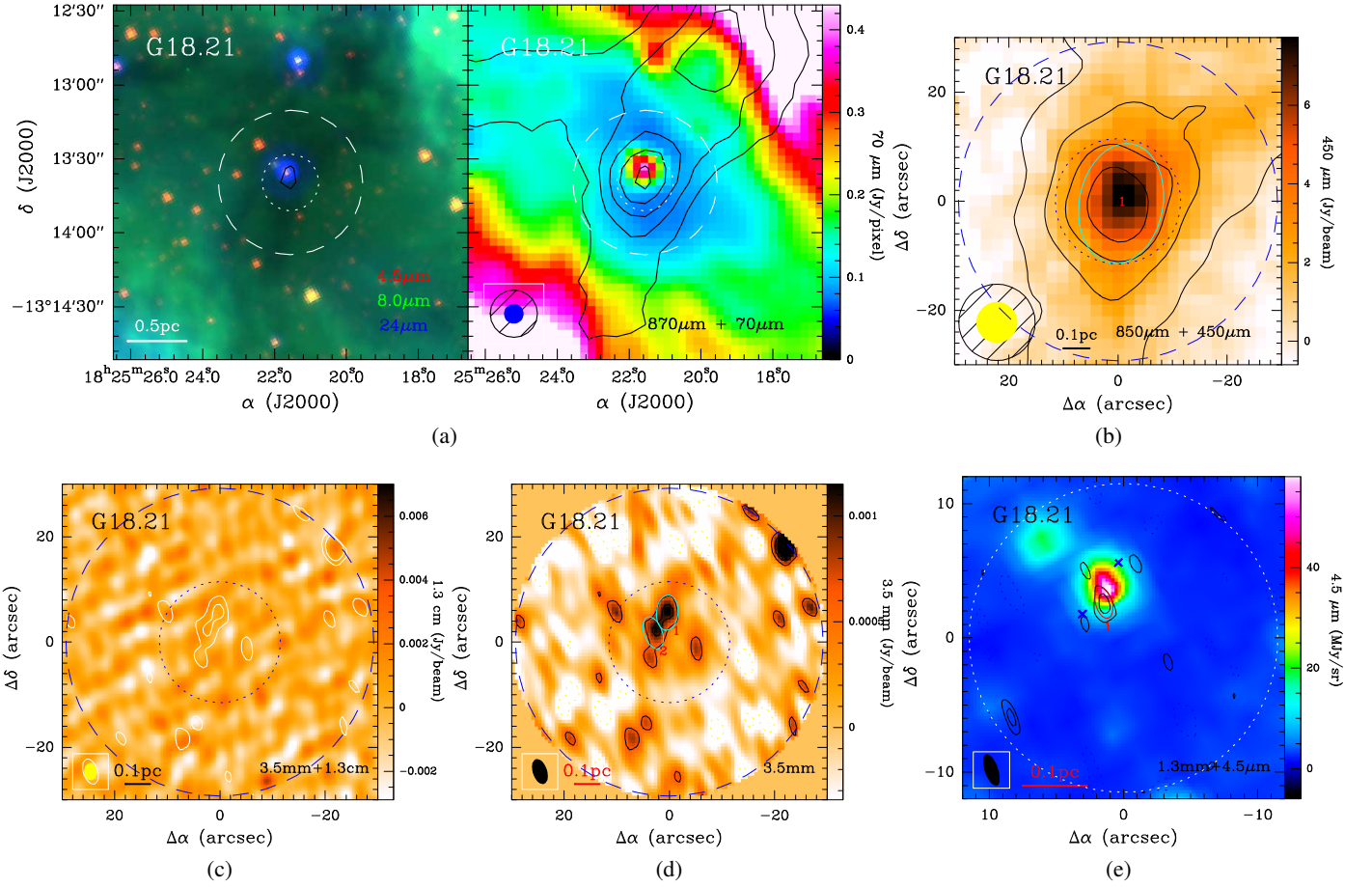


Fig. D.2. G18.21: (a) (left) Three-color image of $4.5\ \mu\text{m}$ (blue), $8.0\ \mu\text{m}$ (green), and $24\ \mu\text{m}$ (red); (right) $870\ \mu\text{m}$ contours overlaid on a $70\ \mu\text{m}$ color scale. The $870\ \mu\text{m}$ contour levels start at 6σ in steps of 7σ ($\sigma = 54\ \text{mJy beam}^{-1}$). (b) $850\ \mu\text{m}$ contours overlaid on a $450\ \mu\text{m}$ color scale. The $850\ \mu\text{m}$ contour levels start at 1.2σ in steps of 4.8σ ($\sigma = 83\ \text{mJy beam}^{-1}$). (c) $3.5\ \text{mm}$ contours overlaid on a $1.3\ \text{cm}$ color scale. For CD configuration observations, (d) the $3.5\ \text{mm}$ contour levels start at -3σ , 3σ in steps of 2σ ($\sigma = 0.20\ \text{mJy beam}^{-1}$), and (e) the $1.3\ \text{mm}$ contour levels start at -3σ , 3σ in steps of 2σ ($\sigma = 1.81\ \text{mJy beam}^{-1}$) superimposed on a $24\ \mu\text{m}$ color scale. The ellipses with numbers indicate the positions of extracted sources. The crosses in the $1.3\ \text{mm}$ CD configuration observations indicate the positions of the corresponding $3.5\ \text{mm}$ CD configuration observations. The dashed and dotted circles in each subfigure indicate the primary beam scales of 3.5 and $1.3\ \text{mm}$ PdBI tracks, respectively.

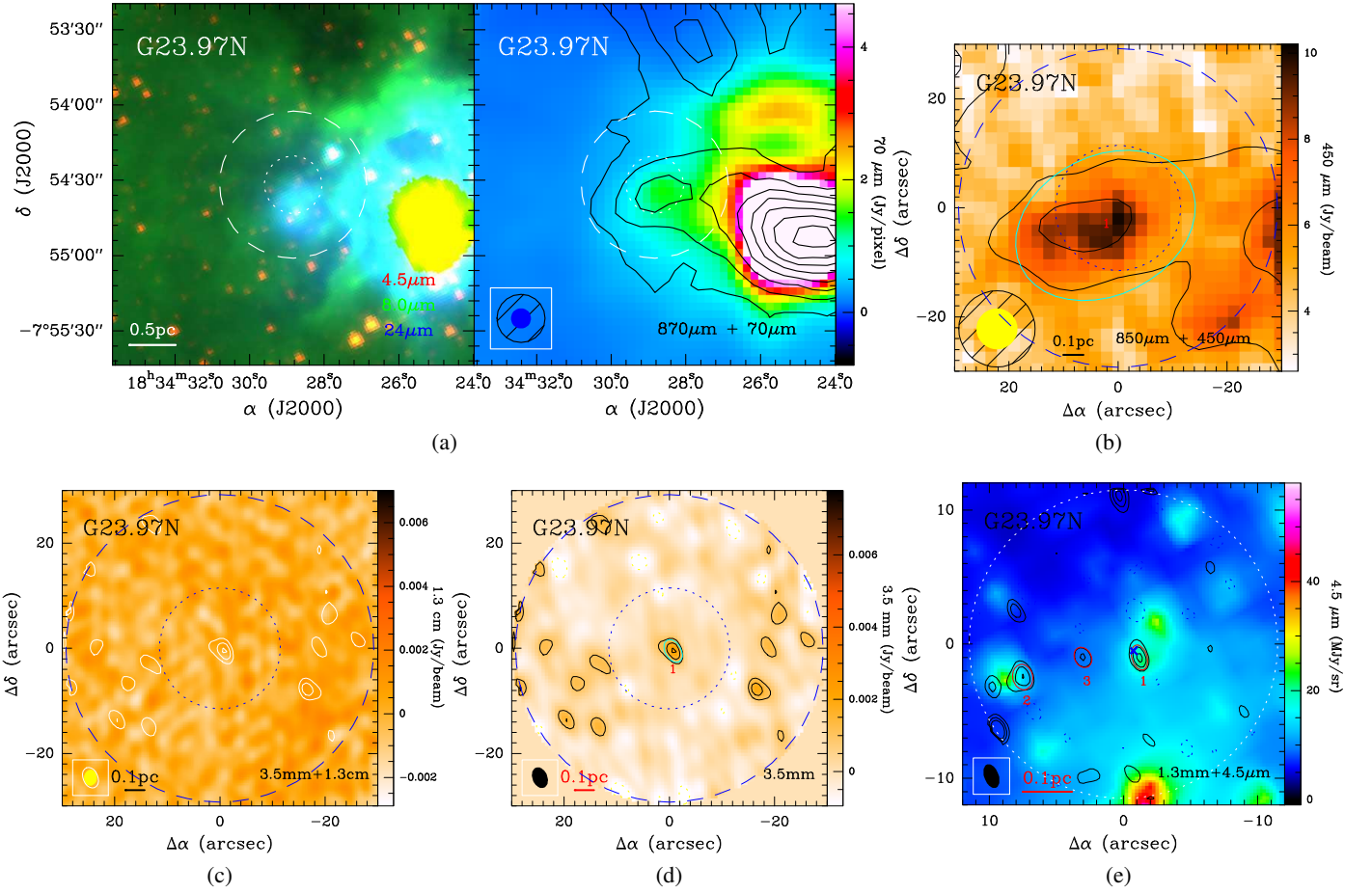


Fig. D.3. G23.97N: (a) (left) Three-color image of $4.5\ \mu\text{m}$ (blue), $8.0\ \mu\text{m}$ (green), and $24\ \mu\text{m}$ (red); (right) $870\ \mu\text{m}$ contours overlaid on a $70\ \mu\text{m}$ color scale. The $870\ \mu\text{m}$ contour levels start at 6σ in steps of 6σ ($\sigma = 54\ \text{mJy beam}^{-1}$). (b) $850\ \mu\text{m}$ contours overlaid on a $450\ \mu\text{m}$ color scale. The $850\ \mu\text{m}$ contour levels start at 3.6σ in steps of 4.8σ ($\sigma = 83\ \text{mJy beam}^{-1}$). (c) $3.5\ \text{mm}$ contours overlaid on a $1.3\ \text{cm}$ color scale. For CD configuration observations, (d) the $3.5\ \text{mm}$ contour levels start at -3σ , 3σ in steps of 1.9σ ($\sigma = 0.32\ \text{mJy beam}^{-1}$), and (e) the $1.3\ \text{mm}$ contour levels start at -3σ , 3σ in steps of 2σ ($\sigma = 1.62\ \text{mJy beam}^{-1}$) superimposed on a $24\ \mu\text{m}$ color scale. The ellipses with numbers indicate the positions of extracted sources. The crosses in the $1.3\ \text{mm}$ CD configuration observations indicate the positions of the corresponding $3.5\ \text{mm}$ CD configuration observations. The dashed and dotted circles in each subfigure indicate the primary beam scales of 3.5 and $1.3\ \text{mm}$ PdBI tracks, respectively.

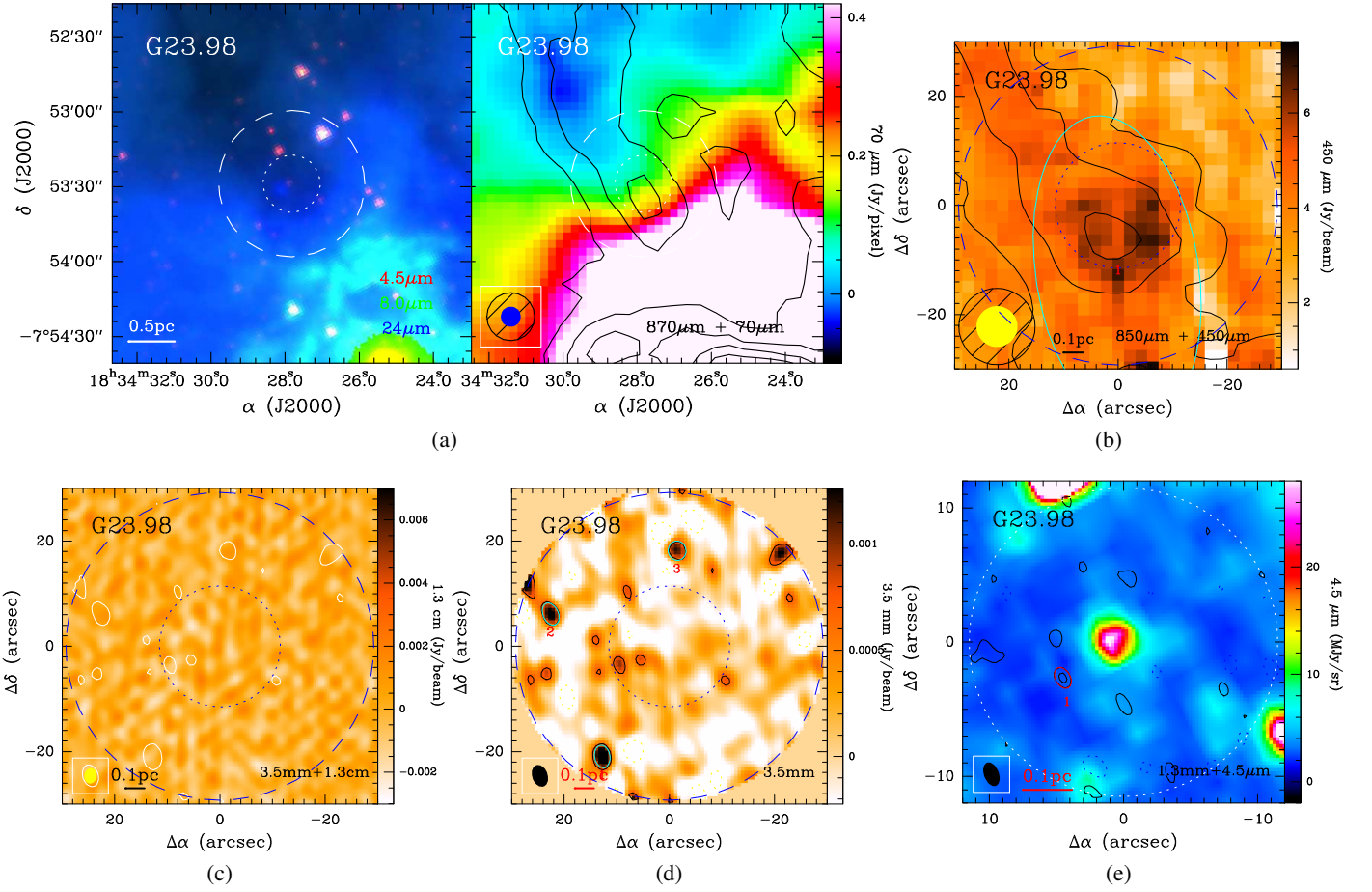


Fig. D.4. G23.98: (a) (left) Three-color image of 4.5 μm (blue), 8.0 μm (green), and 24 μm (red); (right) 870 μm contours overlaid on a 70 μm color scale. The 870 μm contour levels start at 6σ in steps of 6σ ($\sigma = 54 \text{ mJy beam}^{-1}$). (b) 850 μm contours overlaid on a 450 μm color scale. The 850 μm contour levels start at 3.6σ in steps of 4.8σ ($\sigma = 83 \text{ mJy beam}^{-1}$). (c) 3.5 mm contours overlaid on a 1.3 cm color scale. For CD configuration observations, (d) the 3.5 mm contour levels start at -3σ , 3σ in steps of 4σ ($\sigma = 0.22 \text{ mJy beam}^{-1}$), and (e) the 1.3 mm contour levels start at -3σ , 3σ in steps of 2σ ($\sigma = 1.65 \text{ mJy beam}^{-1}$) superimposed on a 24 μm color scale. The ellipses with numbers indicate the positions of extracted sources. The crosses in the 1.3 mm CD configuration observations indicate the positions of the corresponding 3.5 mm CD configuration observations. The dashed and dotted circles in each subfigure indicate the primary beam scales of 3.5 and 1.3 mm PdBI tracks, respectively.

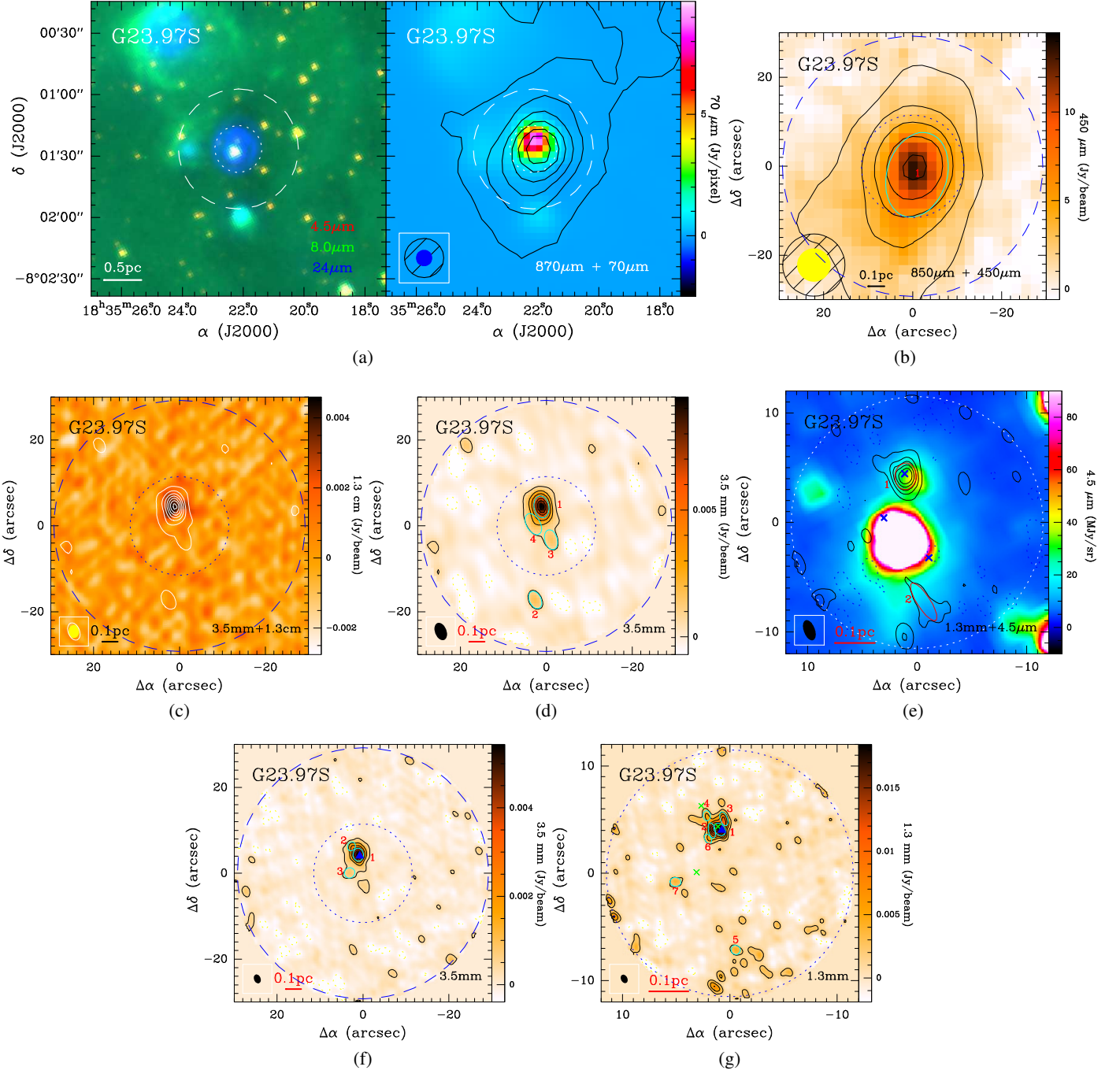


Fig. D.5. G23.97S: (a) (left) Three-color image of $4.5\ \mu\text{m}$ (blue), $8.0\ \mu\text{m}$ (green), and $24\ \mu\text{m}$ (red); (right) $870\ \mu\text{m}$ contours overlaid on a $70\ \mu\text{m}$ color scale. The $870\ \mu\text{m}$ contour levels start at 6σ in steps of 10σ ($\sigma = 54\ \text{mJy beam}^{-1}$). (b) $850\ \mu\text{m}$ contours overlaid on a $450\ \mu\text{m}$ color scale. The $850\ \mu\text{m}$ contour levels start at 6σ in steps of 8σ ($\sigma = 83\ \text{mJy beam}^{-1}$). (c) $3.5\ \text{mm}$ contours overlaid on a $1.3\ \text{cm}$ color scale. For CD configuration observations, (d) the $3.5\ \text{mm}$ contour levels start at -3σ , 3σ in steps of 6σ ($\sigma = 0.23\ \text{mJy beam}^{-1}$), and (e) the $1.3\ \text{mm}$ contour levels start at -3σ , 3σ in steps of 5σ ($\sigma = 1.43\ \text{mJy beam}^{-1}$). For BCD configuration observations, (f) the $3.5\ \text{mm}$ contour levels start at -3σ , 3σ in steps of 6σ ($\sigma = 0.13\ \text{mJy beam}^{-1}$), and (g) the $1.3\ \text{mm}$ contour levels start at -3σ , 3σ in steps of 4σ ($\sigma = 0.64\ \text{mJy beam}^{-1}$) superimposed on a $24\ \mu\text{m}$ color scale. The ellipses with numbers indicate the positions of extracted sources. The crosses in the $1.3\ \text{mm}$ (B)CD configuration observations indicate the peak positions of the corresponding cores and condensations in the $3.5\ \text{mm}$ (B)CD configuration observations. The dashed and dotted circles indicate the primary beam scales of 3.5 and $1.3\ \text{mm}$ PdBI tracks, respectively. The blue triangle “▲” indicates the position of $6668\ \text{MHz}$ methanol masers.

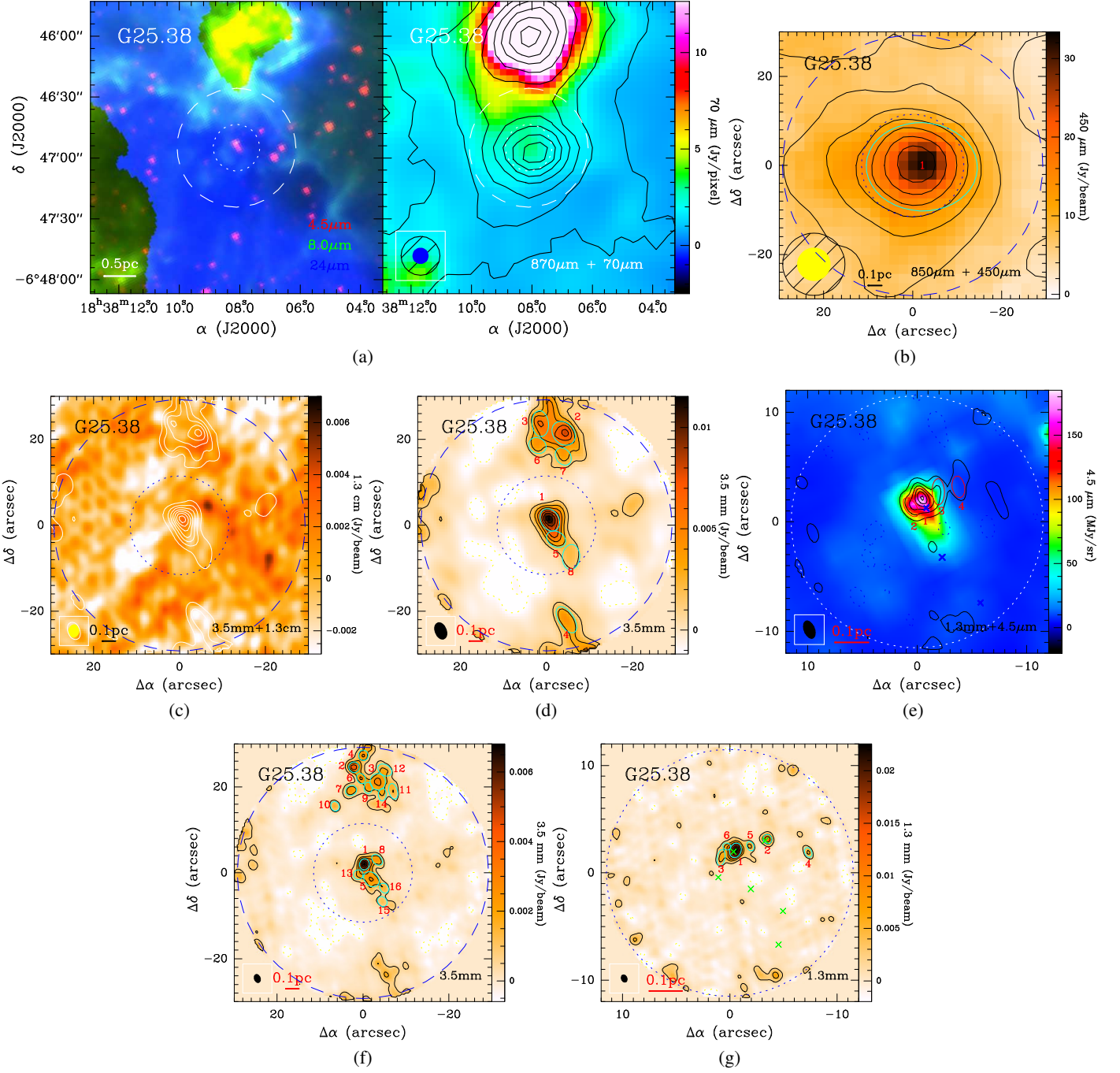


Fig. D.6. G25.38: (a) (left) Three-color image of $4.5\ \mu\text{m}$ (blue), $8.0\ \mu\text{m}$ (green), and $24\ \mu\text{m}$ (red); (right) $870\ \mu\text{m}$ contours overlaid on a $70\ \mu\text{m}$ color scale. The $870\ \mu\text{m}$ contour levels start at 5.3σ in steps of 8.8σ ($\sigma = 61\ \text{mJy beam}^{-1}$). (b) $850\ \mu\text{m}$ contours overlaid on a $450\ \mu\text{m}$ color scale. The $850\ \mu\text{m}$ contour levels start at 6σ in steps of 8σ ($\sigma = 83\ \text{mJy beam}^{-1}$). (c) $3.5\ \text{mm}$ contours overlaid on a $1.3\ \text{cm}$ color scale. For CD configuration observations, (d) the $3.5\ \text{mm}$ contour levels start at -3σ , 3σ in steps of 4σ ($\sigma = 0.39\ \text{mJy beam}^{-1}$), and (e) the $1.3\ \text{mm}$ contour levels start at -3σ , 3σ in steps of 6σ ($\sigma = 1.34\ \text{mJy beam}^{-1}$). For BCD configuration observations, (f) the $3.5\ \text{mm}$ contour levels start at -3σ , 3σ in steps of 5σ ($\sigma = 0.20\ \text{mJy beam}^{-1}$), and (g) the $1.3\ \text{mm}$ contour levels start at -3σ , 3σ in steps of 5σ ($\sigma = 0.66\ \text{mJy beam}^{-1}$) superimposed on a $24\ \mu\text{m}$ color scale. The ellipses with numbers indicate the positions of extracted sources. The crosses in the $1.3\ \text{mm}$ (B)CD configuration observations indicate the peak positions of the corresponding cores and condensations in the $3.5\ \text{mm}$ (B)CD configuration observations. The dashed and dotted circles in each subfigure indicate the primary beam scales of 3.5 and $1.3\ \text{mm}$ PdBI tracks, respectively.

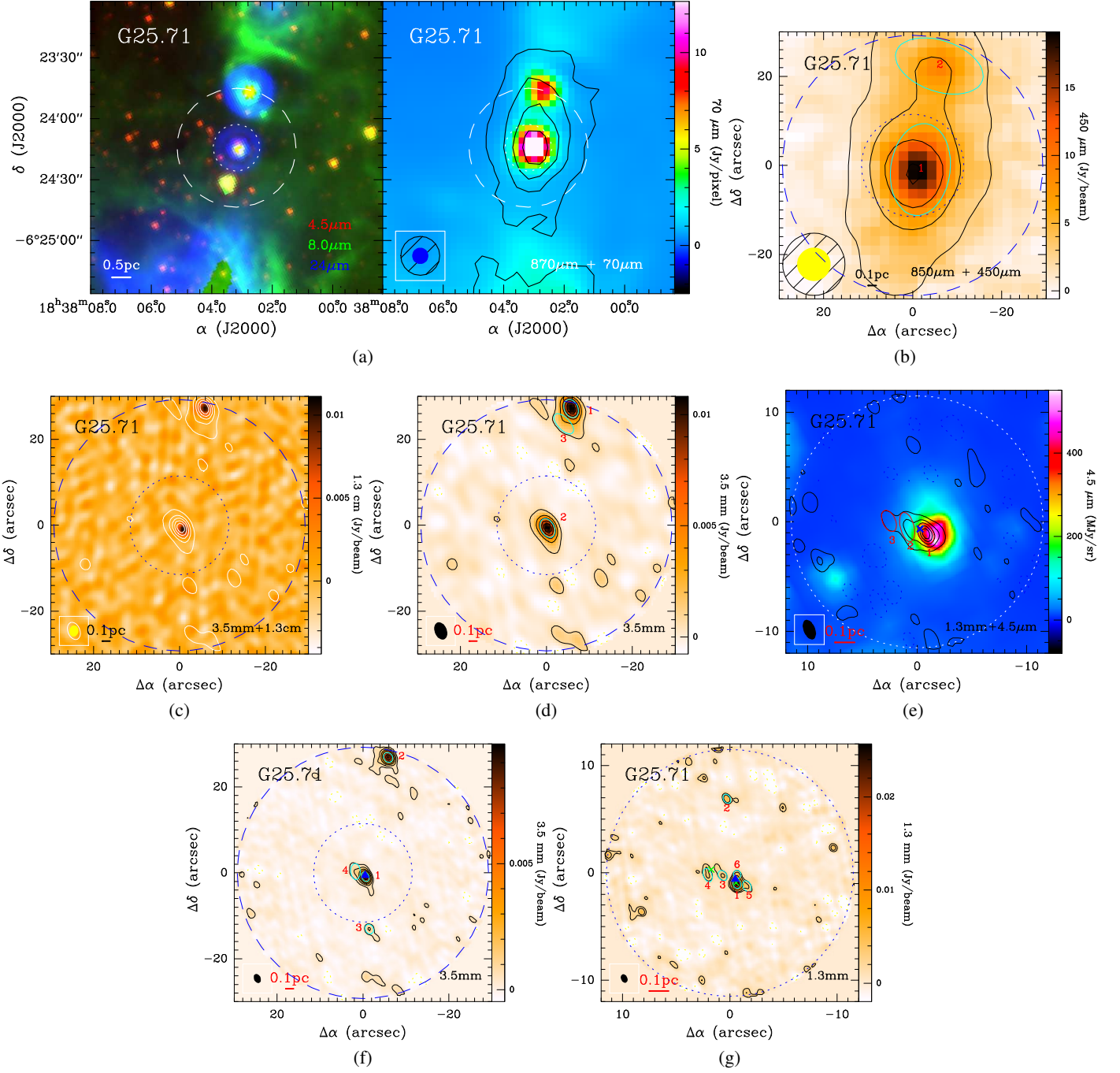


Fig. D.7. G25.71: (a) (left) Three-color image of $4.5\ \mu\text{m}$ (blue), $8.0\ \mu\text{m}$ (green), and $24\ \mu\text{m}$ (red); (right) $870\ \mu\text{m}$ contours overlaid on a $70\ \mu\text{m}$ color scale. The $870\ \mu\text{m}$ contour levels start at 5.3σ in steps of 7σ ($\sigma = 61\ \text{mJy beam}^{-1}$). (b) $850\ \mu\text{m}$ contours overlaid on a $450\ \mu\text{m}$ color scale. The $850\ \mu\text{m}$ contour levels start at 6σ in steps of 8σ ($\sigma = 83\ \text{mJy beam}^{-1}$). (c) $3.5\ \text{mm}$ contours overlaid on a $1.3\ \text{cm}$ color scale. For CD configuration observations, (d) the $3.5\ \text{mm}$ contour levels start at -3σ , 3σ in steps of 8σ ($\sigma = 0.26\ \text{mJy beam}^{-1}$), and (e) the $1.3\ \text{mm}$ contour levels start at -3σ , 3σ in steps of 4σ ($\sigma = 1.34\ \text{mJy beam}^{-1}$). For BCD configuration observations, (f) the $3.5\ \text{mm}$ contour levels are -3σ , 3σ , 7σ , 13σ , 20σ , and to maximum in steps of 13σ ($\sigma = 0.16\ \text{mJy beam}^{-1}$), and (g) the $1.3\ \text{mm}$ contour levels are -3σ , 3σ , 5σ , 10σ and to maximum in steps of 8σ ($\sigma = 0.66\ \text{mJy beam}^{-1}$) superimposed on a $24\ \mu\text{m}$ color scale. The ellipses with numbers indicate the positions of extracted sources. The crosses in the $1.3\ \text{mm}$ (B)CD configuration observations indicate the peak positions of the corresponding cores and condensations in the $3.5\ \text{mm}$ (B)CD configuration observations. The dashed and dotted circles in each subfigure indicate the primary beam scales of 3.5 and $1.3\ \text{mm}$ PdBI tracks, respectively. The blue triangle “▲” indicates the position of $6668\ \text{MHz}$ methanol masers.

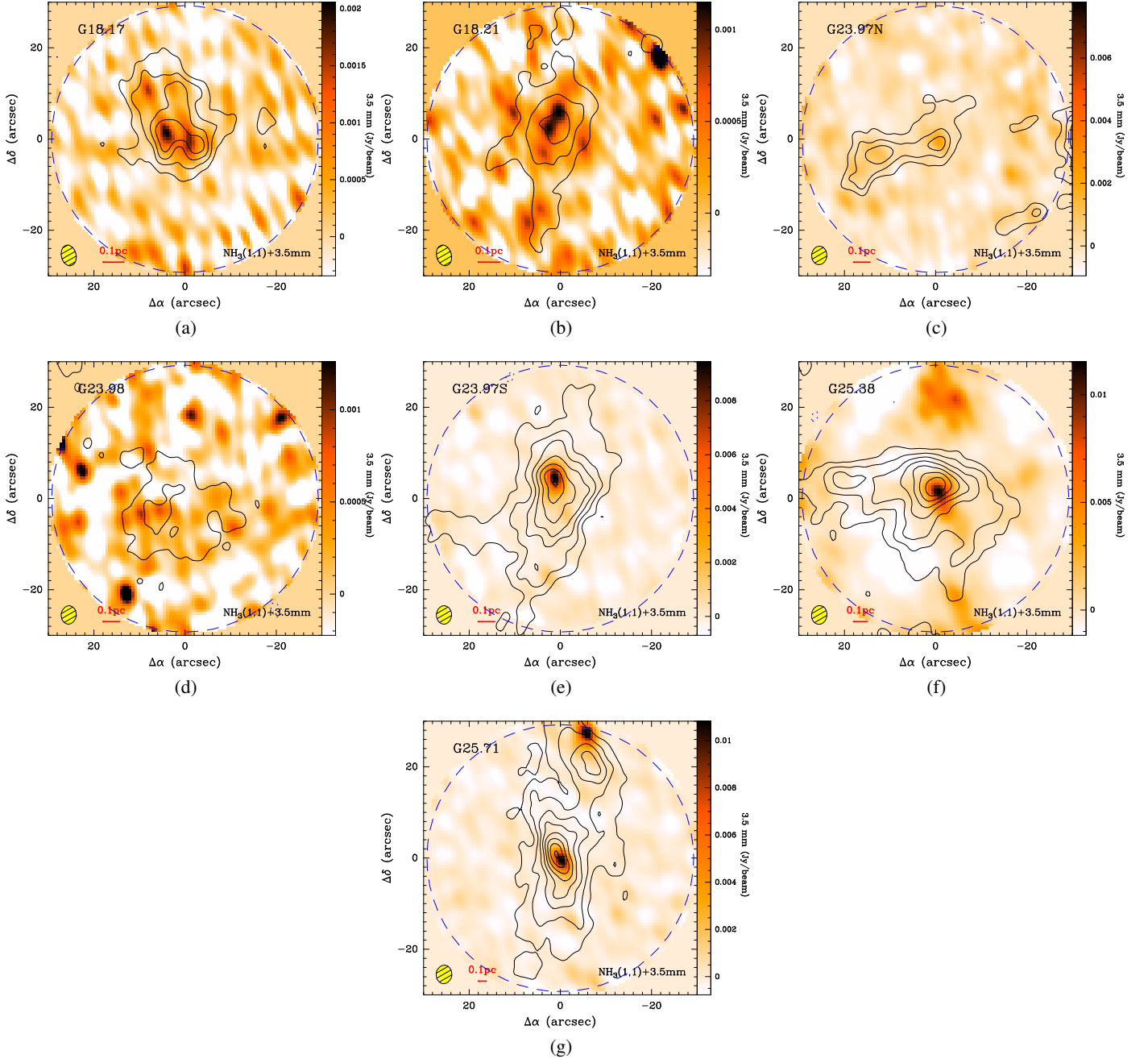


Fig. D.8. $\text{NH}_3(1,1)$ integrated-intensity contours overlaid on a 3.5 mm continuum with velocity range covering only the main line. The contour levels start at -3σ in steps of 3σ for $\text{NH}_3(1,1)$ with $\sigma_{(a)-(g)} = 12.5, 20.2, 9.1, 9.8, 12.6, 12.9, 10.2 \text{ mJy beam}^{-1} \text{ km s}^{-1}$. The synthesized beam size of each subfigure is indicated at the bottom-left corner.

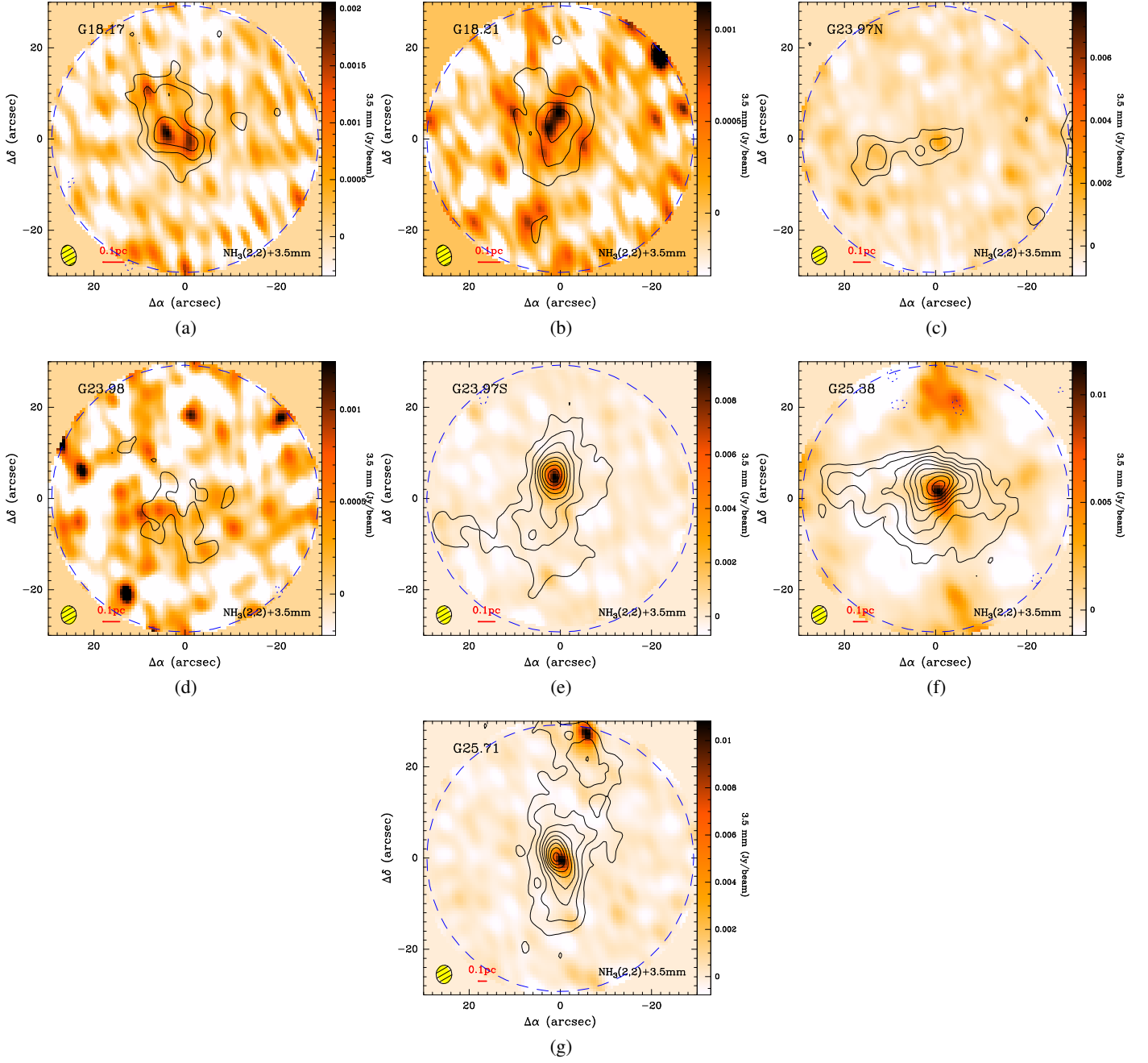


Fig. D.9. $\text{NH}_3(2,2)$ integrated-intensity contours overlaid on a 3.5 mm continuum with velocity range covering only the main line. The contour levels start at -3σ in steps of 3σ for $\text{NH}_3(2,2)$ with $\sigma_{(a)-(g)} = 10.8, 13.5, 7.9, 7.2, 8.2, 9.7, 8.3 \text{ mJy beam}^{-1} \text{ km s}^{-1}$. The synthesized beam size of each subfigure is indicated at the bottom-left corner.

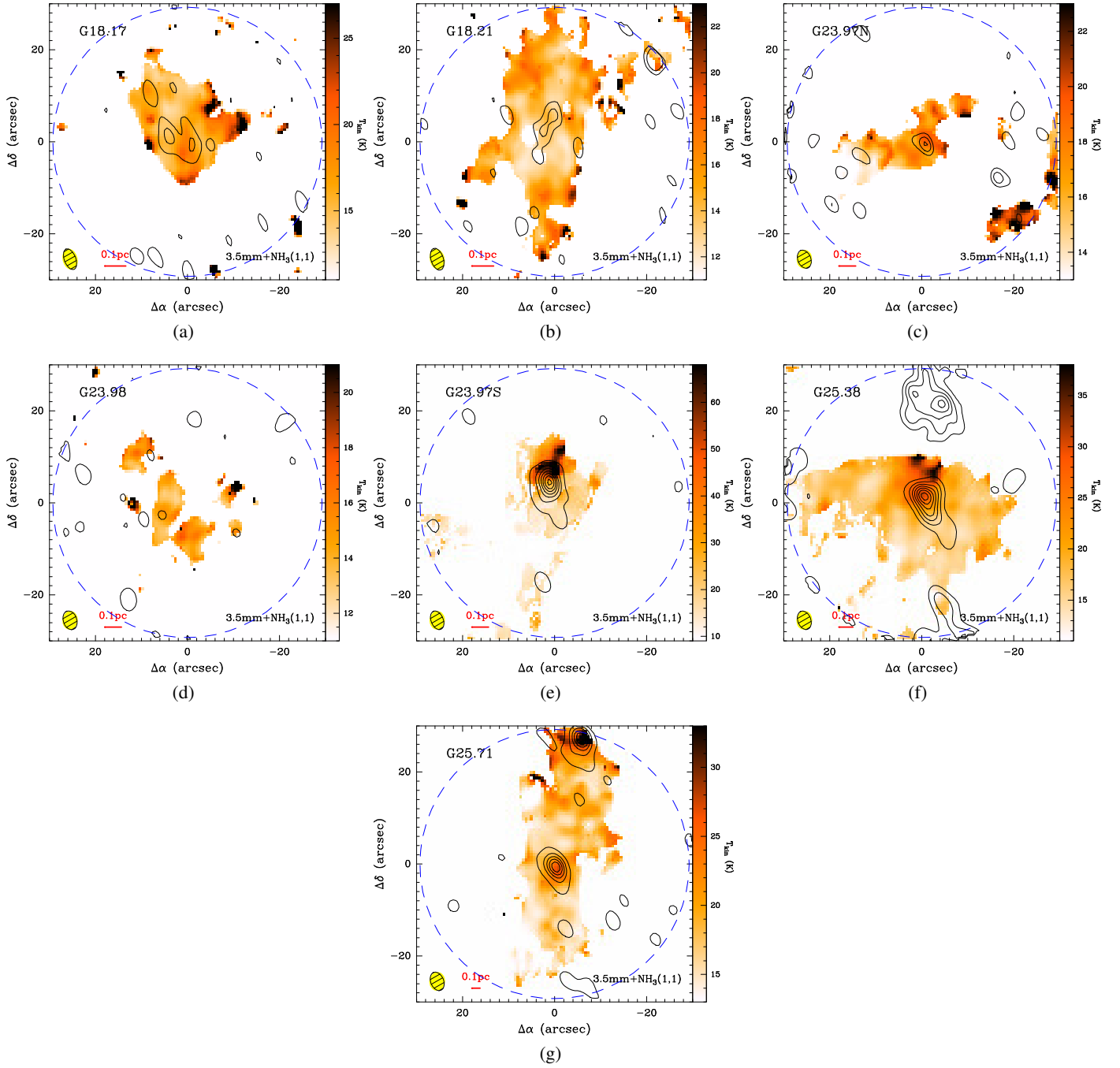


Fig. D.10. The kinetic temperature T_{kin} maps overlaid by 3.5 mm continuum contours. The synthesized beam size of each subfigure is indicated at the bottom-left corner.

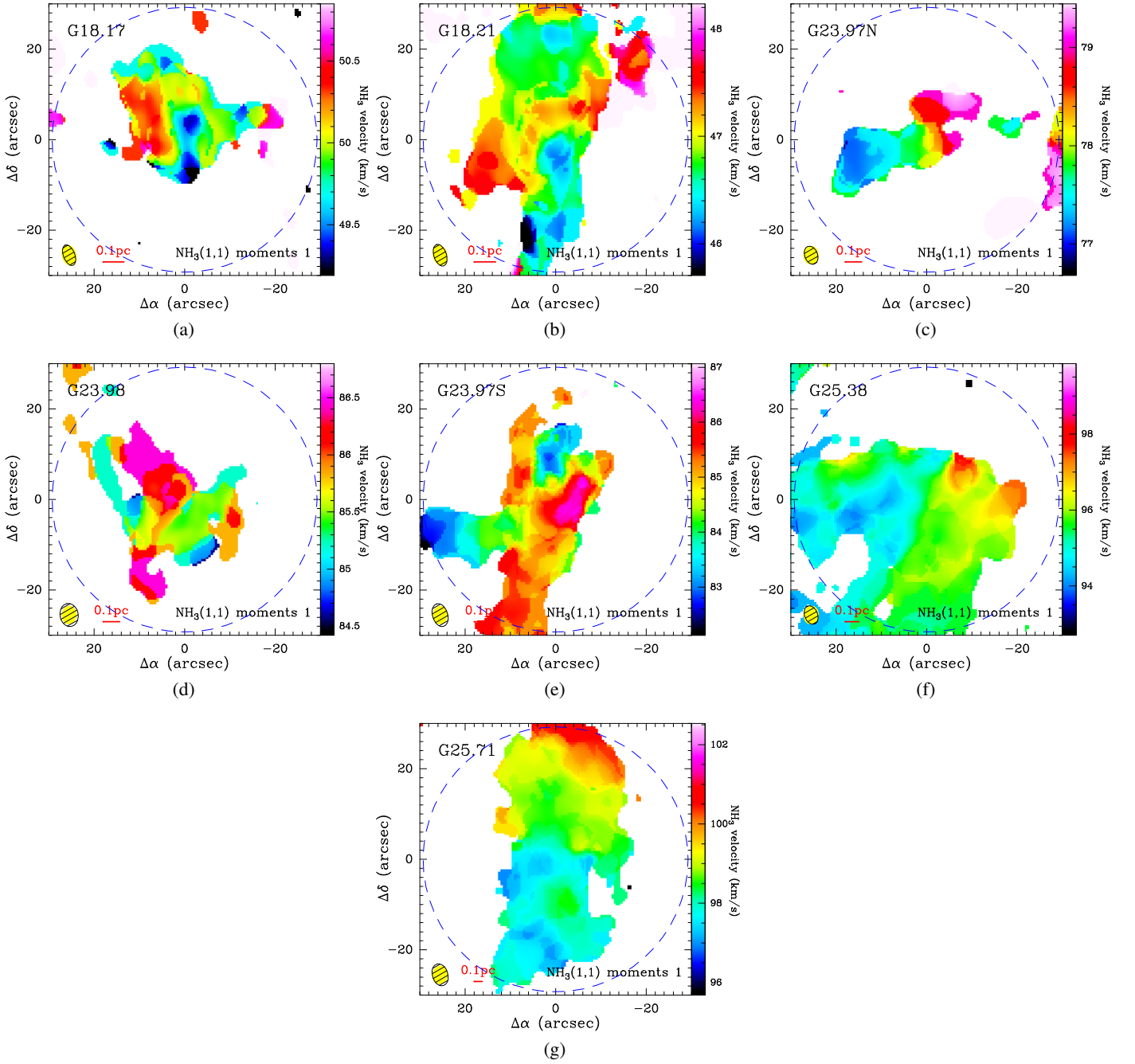


Fig. D.11. Velocity distribution (moment 1) of $\text{NH}_3(1,1)$ line. The synthesized beam size of each subfigure is indicated at the bottom-left corner.

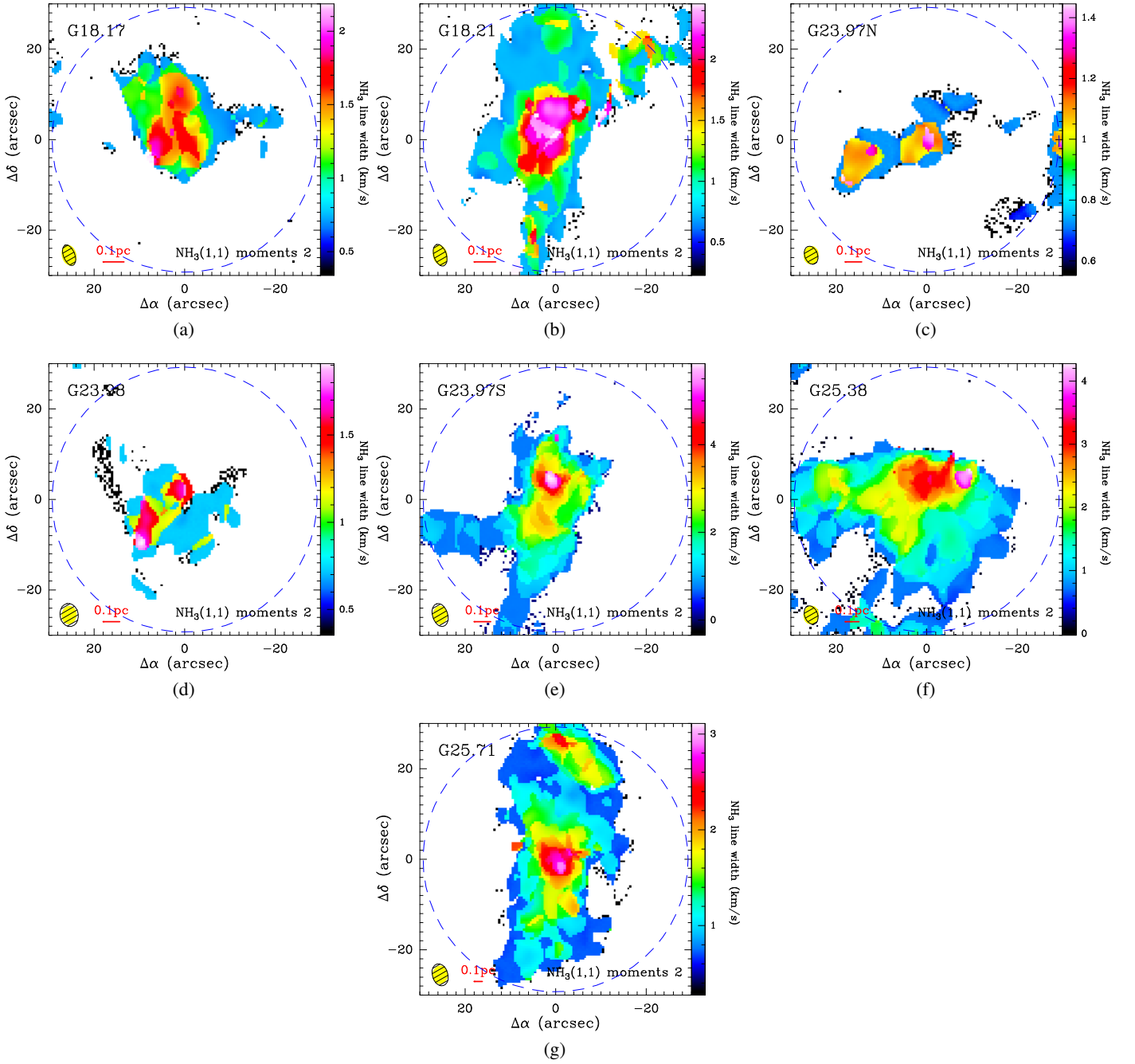


Fig. D.12. Velocity dispersion (moment 2) of $\text{NH}_3(1,1)$ line. The synthesized beam size of each subfigure is indicated at the bottom-left corner.

Table D.1. Clump parameters derived from 450, 850, and 870 μm observations.

Source	No.	Offsets ", "	FWHM "	R_{eff} pc	T_{kin} K	I_{peak} Jy beam $^{-1}$	S_{int} Jy	Mass M_{\odot}	N_{H_2} 10^{23}cm^{-2}	Σ g cm^{-2}	n_{H_2} 10^5cm^{-3}	$\Delta v_{\text{NH}_3(1,1)}$ km s^{-1}	M_{vir} M_{\odot}
450 μm													
G18.17	1	(-0.74, 0.55)	25.54	0.277	16.9 ± 1.3	10.46	128.75	1793.7 ± 303.3	5.8 ± 1.0	1.5 ± 0.3	6.1 ± 1.0	1.40 ± 0.06	48.7 ± 2.0
G18.21	1	(-0.58, -0.40)	17.87	0.187	13.1 ± 0.8	7.80	47.35	1133.7 ± 176.4	8.1 ± 1.3	2.1 ± 0.3	12.6 ± 2.0	1.35 ± 0.06	31.9 ± 1.4
G23.97N	1	(2.29, -3.20)	29.07	0.396	14.8 ± 1.0	10.02	157.61	4667.5 ± 806.8	7.4 ± 1.3	2.0 ± 0.3	5.5 ± 0.9	1.49 ± 0.06	74.1 ± 3.2
G23.98	1	(0.13, -12.17)	37.51	0.511	13.4 ± 0.6	6.98	213.77	8208.8 ± 1028.3	7.9 ± 1.0	2.1 ± 0.3	4.5 ± 0.6	1.37 ± 0.04	87.7 ± 2.8
G23.44	1	(-0.02, -2.10)	20.88	0.357	26.4 ± 2.7	41.24	329.82	4741.1 ± 834.4	9.3 ± 1.6	2.5 ± 0.4	7.6 ± 1.3	2.86 ± 0.02	128.5 ± 0.9
G23.44	2	(-3.59, 11.96)	9.86	0.169	30.7 ± 4.4	12.13	26.50	297.1 ± 68.4	2.6 ± 0.6	0.7 ± 0.2	4.5 ± 1.0	2.66 ± 0.07	56.5 ± 1.5
G23.97S	1	(-0.98, -1.90)	15.72	0.215	23.4 ± 4.6	14.05	65.80	751.3 ± 271.7	4.1 ± 1.5	1.1 ± 0.4	5.5 ± 2.0	2.93 ± 0.07	79.4 ± 1.9
G25.38	1	(-2.06, -0.30)	21.96	0.358	23.2 ± 2.0	32.12	282.88	4639.2 ± 740.4	9.0 ± 1.4	2.4 ± 0.4	7.4 ± 1.2	2.31 ± 0.04	103.9 ± 2.0
G25.71	1	(-1.75, -0.91)	15.89	0.440	19.6 ± 1.1	18.73	92.51	6083.6 ± 689.9	7.9 ± 0.9	2.1 ± 0.2	5.2 ± 0.6	1.88 ± 0.03	104.0 ± 1.7
G25.71	2	(-6.00, 22.35)	14.10	0.390	19.1 ± 2.2	8.19	33.97	2336.9 ± 564.5	3.8 ± 0.9	1.0 ± 0.2	2.9 ± 0.7	1.84 ± 0.04	90.3 ± 2.1
850 μm													
G18.17	1	(-0.58, -0.39)	32.29	0.351	17.3 ± 1.4	2.10	11.66	1095.4 ± 139.7	2.2 ± 0.3	0.6 ± 0.1	1.8 ± 0.2	1.35 ± 0.06	59.2 ± 2.4
G18.21	1	(0.32, -0.51)	21.93	0.230	13.4 ± 0.7	1.60	4.14	554.5 ± 48.5	2.6 ± 0.2	0.7 ± 0.1	3.3 ± 0.3	1.29 ± 0.06	37.1 ± 1.7
G23.97N	1	(10.88, -2.94)	21.90	0.298	14.1 ± 0.4	0.90	2.37	490.1 ± 21.6	1.4 ± 0.1	0.4 ± 0.0	1.3 ± 0.1	1.03 ± 0.01	38.5 ± 0.3
G23.98	1	(0.65, -6.65)	65.61	0.894	12.5 ± 1.0	1.07	24.92	6305.8 ± 942.3	2.0 ± 0.3	0.5 ± 0.1	0.6 ± 0.1	1.57 ± 0.12	176.4 ± 13.2
G23.44	1	(0.07, -0.72)	26.64	0.456	26.3 ± 2.3	7.20	26.66	3376.4 ± 399.9	4.1 ± 0.5	1.1 ± 0.1	2.6 ± 0.3	2.90 ± 0.03	166.2 ± 1.5
G23.97S	1	(-0.74, -0.01)	21.48	0.294	23.4 ± 2.8	3.32	8.36	792.7 ± 133.6	2.3 ± 0.4	0.6 ± 0.1	2.3 ± 0.4	3.16 ± 0.07	117.1 ± 2.7
G23.97S	2	(9.60, -25.16)	23.19	0.317	15.5 ± 1.2	0.67	2.41	426.9 ± 55.5	1.1 ± 0.1	0.3 ± 0.0	1.0 ± 0.1	1.34 ± 0.04	53.2 ± 1.5
G25.38	1	(0.11, -0.39)	28.01	0.457	22.0 ± 1.8	4.92	19.70	2904.9 ± 332.4	3.5 ± 0.4	0.9 ± 0.1	2.2 ± 0.3	2.22 ± 0.05	127.2 ± 2.8
G25.71	1	(0.22, -2.80)	22.97	0.635	19.0 ± 0.9	2.58	8.30	4351.0 ± 322.2	2.7 ± 0.2	0.7 ± 0.1	1.2 ± 0.1	1.74 ± 0.02	138.9 ± 1.8
G25.71	2	(-6.01, 24.50)	21.49	0.594	20.0 ± 2.9	0.76	2.51	1223.5 ± 261.0	0.9 ± 0.2	0.2 ± 0.0	0.4 ± 0.1	2.02 ± 0.05	151.0 ± 3.8
870 μm													
G18.17	1	(2.15, 0.47)	27.47	0.298	16.9 ± 1.2	1.91	3.91	387.3 ± 43.9	1.1 ± 0.1	0.3 ± 0.0	1.1 ± 0.1	1.39 ± 0.05	52.2 ± 2.0
G18.21	1	(2.36, 1.64)	28.28	0.296	13.4 ± 0.5	1.70	3.70	501.8 ± 31.5	1.4 ± 0.1	0.4 ± 0.0	1.4 ± 0.1	1.19 ± 0.04	44.1 ± 1.7
G23.97N	1	(1.27, -2.44)	23.95	0.326	15.1 ± 1.1	0.78	1.22	227.5 ± 27.3	0.5 ± 0.1	0.1 ± 0.0	0.5 ± 0.1	1.47 ± 0.06	60.4 ± 2.6
G23.98	1	(0.23, -3.16)	25.89	0.353	14.3 ± 0.6	0.70	1.26	258.1 ± 19.2	0.5 ± 0.0	0.1 ± 0.0	0.4 ± 0.0	1.40 ± 0.02	61.8 ± 0.9
G23.44	1	(-3.76, -0.61)	27.59	0.472	27.1 ± 2.7	5.85	12.09	1498.6 ± 196.1	1.7 ± 0.2	0.4 ± 0.1	1.0 ± 0.1	2.94 ± 0.02	174.9 ± 1.4
G23.97S	1	(0.66, -0.59)	28.41	0.389	22.7 ± 2.1	3.20	7.00	708.3 ± 94.3	1.2 ± 0.2	0.3 ± 0.0	0.9 ± 0.1	3.02 ± 0.06	148.0 ± 2.7
G25.38	1	(0.78, -1.71)	27.56	0.449	21.5 ± 1.6	3.39	6.98	1080.6 ± 115.2	1.3 ± 0.1	0.4 ± 0.0	0.9 ± 0.1	2.20 ± 0.05	124.5 ± 2.9
G25.71	1	(-0.99, 2.06)	29.66	0.820	18.8 ± 1.2	1.76	4.19	2279.1 ± 225.6	0.8 ± 0.1	0.2 ± 0.0	0.3 ± 0.0	1.75 ± 0.03	180.9 ± 3.4

Table D.2. Fragment parameters derived from PdBI 3.5 mm observations.

Source	No.	Offsets ", "	FWHM "	R_{eff} pc	T_{kin} K	I_{peak} mJy beam ⁻¹	S_{int}^* mJy	Mass M_{\odot}	N_{H_2} 10 ²³ cm ⁻²	Σ g cm ⁻²	n_{H_2} 10 ⁶ cm ⁻³	$\Delta v_{\text{NH}_3(1,1)}$ km s ⁻¹	M_{vir} M_{\odot}
CD configuration observations													
G18.17	1	(3.96, 1.14)	4.13	0.045	16.2 ± 1.9	1.99	3.44	35.4 ± 4.7	4.4 ± 0.6	1.2 ± 0.2	2.9 ± 0.4	1.32 ± 0.04	7.4 ± 0.2
G18.17	2	(-1.05, -0.69)	4.13	0.045	18.8 ± 2.2	1.73	3.41	29.7 ± 4.0	3.7 ± 0.5	1.0 ± 0.1	2.4 ± 0.3	1.40 ± 0.06	7.9 ± 0.3
G18.17	3	(8.06, 10.63)	3.25	0.035	16.6 ± 1.3	1.55	1.76	17.6 ± 1.5	3.5 ± 0.3	0.9 ± 0.1	2.9 ± 0.3	1.07 ± 0.07	4.7 ± 0.3
G18.21	1	(0.39, 5.62)	4.98	0.052	14.6 ± 1.9	1.21	2.51	27.0 ± 4.0	2.5 ± 0.4	0.7 ± 0.1	1.4 ± 0.2	1.49 ± 0.06	9.8 ± 0.4
G18.21	2	(3.06, 1.77)	4.29	0.045	14.4 ± 1.4	0.85	1.39	15.3 ± 1.7	1.9 ± 0.2	0.5 ± 0.1	1.2 ± 0.1	1.65 ± 0.04	9.3 ± 0.2
G23.97N	1	(-0.74, -0.49)	3.57	0.049	17.7 ± 1.4	2.19	2.64	38.7 ± 3.4	4.1 ± 0.4	1.1 ± 0.1	2.4 ± 0.2	1.28 ± 0.06	7.8 ± 0.4
G23.44	1*	(0.09, -2.43)	4.08	0.070	40.1 ± 17.3	7.83	11.01 ^{40.8%}	42.9 ± 19.4	2.2 ± 1.0	0.6 ± 0.3	0.9 ± 0.4	3.66 ± 0.03	32.2 ± 0.3
G23.44	2	(-0.80, 10.11)	4.55	0.078	31.7 ± 5.6	4.65	8.46	103.7 ± 19.6	4.3 ± 0.8	1.1 ± 0.2	1.6 ± 0.3	2.66 ± 0.07	26.0 ± 0.7
G23.44	3	(-4.15, -3.94)	4.08	0.070	30.1 ± 10.0	1.67	2.26	29.3 ± 10.4	1.5 ± 0.5	0.4 ± 0.1	0.6 ± 0.2	2.60 ± 0.10	22.9 ± 0.9
G23.44	4	(2.73, -4.45)	3.61	0.062	46.7 ± 18.1	1.42	1.75	14.2 ± 5.8	0.9 ± 0.4	0.2 ± 0.1	0.4 ± 0.2	3.83 ± 0.10	29.8 ± 0.8
G23.44	5	(-0.11, 2.10)	4.89	0.084	27.3 ± 7.2	1.43	2.96	42.6 ± 12.0	1.5 ± 0.4	0.4 ± 0.1	0.5 ± 0.1	3.23 ± 0.04	34.0 ± 0.4
G23.44	6	(-4.79, 9.20)	3.62	0.062	27.5 ± 4.5	1.29	1.52	21.7 ± 3.8	1.4 ± 0.2	0.4 ± 0.1	0.7 ± 0.1	2.66 ± 0.04	20.7 ± 0.3
G23.97S	1*	(1.13, 4.45)	4.04	0.055	44.4 ± 15.3	9.43	14.71 ^{21.7%}	17.5 ± 6.3	1.4 ± 0.5	0.4 ± 0.1	0.8 ± 0.3	5.16 ± 0.32	35.9 ± 2.2
G23.97S	2	(2.60, -17.24)	3.25	0.044	15.8 ± 1.5	1.76	1.81	30.4 ± 3.3	3.8 ± 0.4	1.0 ± 0.1	2.5 ± 0.3	1.43 ± 0.13	8.0 ± 0.7
G23.97S	3	(-1.07, -3.21)	3.52	0.048	18.2 ± 3.3	1.50	1.83	26.3 ± 5.4	2.8 ± 0.6	0.8 ± 0.2	1.7 ± 0.3	1.70 ± 0.09	10.3 ± 0.6
G23.97S	4	(3.04, 0.42)	3.89	0.053	20.6 ± 4.1	1.44	2.19	27.4 ± 6.0	2.4 ± 0.5	0.6 ± 0.1	1.3 ± 0.3	3.00 ± 0.04	20.1 ± 0.3
G25.38	1	(-0.81, 1.26)	4.74	0.077	32.2 ± 6.1	11.29	22.36	244.5 ± 49.5	10.2 ± 2.1	2.7 ± 0.6	3.9 ± 0.8	2.53 ± 0.04	24.5 ± 0.4
G25.38	2	(-4.01, 21.42)	5.41	0.088	18.7 ± 4.9	7.88	20.04	396.3 ± 115.8	12.7 ± 3.7	3.4 ± 1.0	4.2 ± 1.2	2.53 ± 0.32	28.1 ± 3.6
G25.38	3	(1.40, 23.66)	4.62	0.075	19.0 ± 1.9	5.80	11.57	223.8 ± 24.3	9.9 ± 1.1	2.6 ± 0.3	3.8 ± 0.4	1.03 ± 0.14	9.7 ± 1.3
G25.38	4	(-4.68, -21.99)	4.44	0.072	14.2 ± 0.8	4.25	8.86	239.1 ± 14.8	11.4 ± 0.7	3.0 ± 0.2	4.6 ± 0.3	1.03 ± 0.14	9.3 ± 1.3
G25.38	5	(-2.28, -3.24)	4.00	0.065	17.9 ± 1.9	4.13	5.85	121.2 ± 14.4	7.1 ± 0.8	1.9 ± 0.2	3.2 ± 0.4	1.24 ± 0.04	10.1 ± 0.4
G25.38	6	(2.08, 18.57)	3.86	0.063	24.4 ± 9.6	3.37	4.32	63.7 ± 27.4	4.0 ± 1.7	1.1 ± 0.5	1.9 ± 0.8	1.24 ± 0.04	9.7 ± 0.4
G25.38	7	(-3.94, 16.02)	3.80	0.062	19.6 ± 4.3	3.08	3.89	72.9 ± 17.9	4.7 ± 1.2	1.3 ± 0.3	2.2 ± 0.5	2.02 ± 0.37	15.8 ± 2.9
G25.38	8	(-5.76, -7.39)	4.70	0.077	17.4 ± 1.7	2.10	4.21	90.4 ± 10.1	3.8 ± 0.4	1.0 ± 0.1	1.5 ± 0.2	1.20 ± 0.04	11.5 ± 0.3
G25.71	1*	(-5.76, 27.18)	3.66	0.101	33.0 ± 8.5	11.47	13.70 ^{11.6%}	48.6 ± 13.4	1.2 ± 0.3	0.3 ± 0.1	0.3 ± 0.1	1.63 ± 0.17	20.6 ± 2.2
G25.71	2*	(-0.27, -0.65)	3.67	0.102	23.6 ± 4.4	11.04	13.56 ^{16.1%}	96.1 ± 19.4	2.3 ± 0.5	0.6 ± 0.1	0.7 ± 0.1	2.30 ± 0.04	29.3 ± 0.6
G25.71	3	(-4.05, 23.64)	3.61	0.100	23.5 ± 3.3	2.11	2.98	131.5 ± 20.3	3.3 ± 0.5	0.9 ± 0.1	1.0 ± 0.1	1.69 ± 0.06	21.2 ± 0.8
BCD configuration observations													
G23.44	1*	(-0.05, -2.81)	2.59	0.044	58.9 ± 53.9	4.80	10.58 ^{40.8%}	27.6 ± 26.1	3.5 ± 3.3	0.9 ± 0.9	2.3 ± 2.2	3.71 ± 0.04	20.7 ± 0.2
G23.44	2	(-0.80, 10.48)	2.22	0.038	32.9 ± 6.6	2.89	4.69	55.2 ± 11.8	9.6 ± 2.0	2.5 ± 0.5	7.3 ± 1.6	2.52 ± 0.08	12.0 ± 0.4
G23.44	3	(-1.10, 7.91)	2.04	0.035	29.5 ± 4.5	1.21	1.60	21.1 ± 3.5	4.3 ± 0.7	1.2 ± 0.2	3.6 ± 0.6	2.63 ± 0.08	11.5 ± 0.4
G23.44	4	(0.86, -0.13)	2.01	0.034	27.6 ± 5.5	1.28	1.59	22.6 ± 4.8	4.8 ± 1.0	1.3 ± 0.3	4.0 ± 0.9	3.66 ± 0.03	15.8 ± 0.1
G23.44	5	(-4.03, 8.96)	2.21	0.038	27.8 ± 3.8	1.09	1.71	24.0 ± 3.5	4.2 ± 0.6	1.1 ± 0.2	3.2 ± 0.5	2.79 ± 0.06	13.3 ± 0.3
G23.44	6	(-0.10, 2.04)	2.15	0.037	28.8 ± 7.6	0.82	1.23	16.7 ± 4.8	3.1 ± 0.9	0.8 ± 0.2	2.4 ± 0.7	3.35 ± 0.05	15.5 ± 0.2
G23.97S	1*	(1.09, 4.35)	2.67	0.037	37.3 ± 9.7	5.56	12.22 ^{21.7%}	17.5 ± 4.8	3.3 ± 0.9	0.9 ± 0.2	2.6 ± 0.7	5.36 ± 0.33	24.7 ± 1.5
G23.97S	2	(2.66, 6.29)	1.96	0.027	34.8 ± 7.9	1.46	1.72	12.2 ± 2.9	4.2 ± 1.0	1.1 ± 0.3	4.6 ± 1.1	4.57 ± 0.41	15.4 ± 1.4
G23.97S	3	(3.10, 0.10)	2.43	0.033	20.0 ± 3.6	0.81	1.45	18.7 ± 3.7	4.2 ± 0.8	1.1 ± 0.2	3.7 ± 0.7	2.95 ± 0.04	12.3 ± 0.2
G25.38	1	(-0.34, 1.97)	2.44	0.040	34.8 ± 7.4	6.60	11.78	118.6 ± 26.8	18.7 ± 4.2	5.0 ± 1.1	13.7 ± 3.1	2.68 ± 0.04	13.4 ± 0.2
G25.38	2	(2.09, 24.60)	2.45	0.040	19.1 ± 2.3	4.32	7.71	149.0 ± 20.3	23.3 ± 3.2	6.2 ± 0.8	17.0 ± 2.3	1.11 ± 0.10	5.6 ± 0.5
G25.38	3	(-3.46, 21.19)	3.72	0.061	18.3 ± 1.2	2.87	11.87	239.4 ± 17.3	16.3 ± 1.2	4.3 ± 0.3	7.8 ± 0.6	1.12 ± 0.09	8.5 ± 0.7
G25.38	4	(-0.10, 27.37)	2.32	0.038	17.7 ± 3.8	2.71	4.36	91.7 ± 22.1	16.0 ± 3.9	4.3 ± 1.0	12.3 ± 3.0	1.14 ± 0.07	5.4 ± 0.4
G25.38	5	(-1.96, -1.50)	3.46	0.056	23.4 ± 3.5	2.70	9.99	153.9 ± 24.8	12.1 ± 1.9	3.2 ± 0.5	6.2 ± 1.0	1.64 ± 0.05	11.6 ± 0.4
G25.38	6	(0.43, 21.97)	2.18	0.036	18.5 ± 2.7	2.62	3.82	76.5 ± 12.6	15.1 ± 2.5	4.0 ± 0.7	12.4 ± 2.0	1.15 ± 0.07	5.1 ± 0.3
G25.38	7	(2.77, 19.17)	2.49	0.041	17.7 ± 2.0	2.45	4.60	96.2 ± 12.4	14.6 ± 1.9	3.9 ± 0.5	10.5 ± 1.4	1.16 ± 0.07	5.9 ± 0.4
G25.38	8	(-3.31, 3.02)	2.34	0.038	23.5 ± 4.5	2.46	4.31	66.2 ± 13.7	11.4 ± 2.4	3.0 ± 0.6	8.7 ± 1.8	2.47 ± 0.04	11.9 ± 0.2
G25.38	9	(-1.22, 19.79)	2.17	0.035	17.7 ± 3.1	1.75	2.59	54.1 ± 10.6	10.8 ± 2.1	2.9 ± 0.6	8.9 ± 1.7	1.17 ± 0.06	5.2 ± 0.2
G25.38	10	(6.51, 15.51)	2.08	0.034	17.5 ± 1.0	1.57	2.05	43.7 ± 2.7	9.5 ± 0.6	2.5 ± 0.2	8.2 ± 0.5	1.18 ± 0.04	5.0 ± 0.2
G25.38	11	(-7.06, 18.99)	2.49	0.041	17.7 ± 3.5	1.50	3.33	69.6 ± 15.4	10.6 ± 2.3	2.8 ± 0.6	7.6 ± 1.7	1.19 ± 0.04	6.0 ± 0.2
G25.38	12	(-5.11, 23.95)	2.88	0.047	17.5 ± 3.1	1.45	3.81	81.0 ± 16.1	9.2 ± 1.8	2.4 ± 0.5	5.7 ± 1.1	1.14 ± 0.07	6.7 ± 0.4
G25.38	13	(1.08, -0.43)	2.27	0.037	26.8 ± 3.2	1.40	2.14	28.4 ± 3.6	5.2 ± 0.7	1.4 ± 0.2	4.1 ± 0.5	2.18 ± 0.07	10.1 ± 0.3
G25.38	14	(-4.51, 18.23)	2.21	0.036	18.8 ± 2.1	1.33	2.14	41.9 ± 5.3	8.1 ± 1.0	2.1 ± 0.3	6.5 ± 0.8	1.12 ± 0.04	5.1 ± 0.2
G25.38	15	(-4.54, -6.68)	2.23	0.036	16.7 ± 1.8	1.16	1.76	39.4 ± 4.8	7.5 ± 0.9	2.0 ± 0.2	6.0 ± 0.7	1.26 ± 0.06	5.8 ± 0.3
G25.38	16	(-4.95, -3.56)	2.14	0.035	18.2 ± 1.2	1.32	1.87	38.1 ± 2.8	7.8 ± 0.6	2.1 ± 0.2	6.5 ± 0.5	1.18 ± 0.09	5.1 ± 0.4
G25.71	1*	(-0.58, -0.92)	1.89	0.052	25.3 ± 5.9	9.72	10.86 ^{16.1%}	71.2 ± 17.8	6.5 ± 1.6	1.7 ± 0.4	3.6 ± 0.9	2.45 ± 0.06	16.1 ± 0.4
G25.71	2*	(-5.86, 26.88)	2.18	0.060	31.6 ± 13.7	9.20	13.10 ^{11.6%}	48.8 ± 22.6	3.4 ± 1.6	0.9 ± 0.4	1.6 ± 0.7	1.77 ± 0.16	13.4 ± 1.2
G25.71	3	(-1.50, -13.11)	2.06	0.057	17.7 ± 1.8	1.19	1.52	91.6 ± 10.7	7.1 ± 0.8	1.9 ± 0.2	3.6 ± 0.4	1.03 ± 0.00	7.3 ± 0.0
G25.71	4	(1.73, 0.31)	2.72	0.075	23.2 ± 3.0	1.17	2.88	128.9 ± 18.4	5.7 ± 0.8	1.5 ± 0.2	2.2 ± 0.3	1.98 ± 0.04	18.7 ± 0.3

(*) The contributions from dust emission are following a measured total flux, e.g., 40.8% of the 3.5 mm flux for G23.44-1 is from dust emission. This was estimated by SED fitting (see Figure A.1).

(†) The sources G23.44-1, G23.97S-1, G25.71-1, and G25.71-2 are clearly associated with compact H II regions.

Table D.3. Fragment parameters derived from PdBI 1.3 mm observations.

Source	No.	Offsets ", "	FWHM "	R_{eff} pc	T_{kin} K	I_{peak} mJy beam $^{-1}$	S_{int} mJy	Mass M_{\odot}	N_{H_2} 10^{23}cm^{-2}	Σ g cm^{-2}	n_{H_2} 10^6cm^{-3}	$\Delta v_{\text{NH}_3(1,1)}$ km s^{-1}	M_{vir} M_{\odot}
CD configuration observations													
G18.17	1	(-1.79, -4.01)	1.29	0.014	19.1 ± 1.8	10.81	11.01	3.8 ± 0.5	4.9 ± 0.6	1.3 ± 0.2	10.1 ± 1.3	1.52 ± 0.07	2.7 ± 0.1
G18.21	1	(1.46, 2.60)	1.55	0.016	15.4 ± 1.9	11.61	13.72	5.9 ± 1.0	5.6 ± 0.9	1.5 ± 0.2	10.0 ± 1.7	1.65 ± 0.07	3.4 ± 0.1
G23.97N	1	(-1.19, -0.99)	1.38	0.019	17.9 ± 1.3	12.39	13.58	8.1 ± 0.8	5.7 ± 0.6	1.5 ± 0.2	8.9 ± 0.9	1.25 ± 0.06	2.9 ± 0.2
G23.97N	2	(7.51, -2.45)	1.67	0.023	25.2 ± 1.9	11.12	16.07	6.2 ± 0.6	3.0 ± 0.3	0.8 ± 0.1	3.8 ± 0.4	1.03 ± 0.01	2.9 ± 0.0
G23.97N	3	(3.02, -0.99)	1.38	0.019	18.0 ± 1.6	8.64	8.66	5.1 ± 0.6	3.6 ± 0.4	1.0 ± 0.1	5.6 ± 0.7	1.03 ± 0.01	2.4 ± 0.0
G23.98	1	(4.52, -2.66)	1.31	0.018	16.6 ± 2.1	10.05	10.07	6.7 ± 1.1	5.2 ± 0.9	1.4 ± 0.2	8.5 ± 1.4	1.12 ± 0.06	2.5 ± 0.1
G23.44	1	(-0.07, -3.26)	2.59	0.044	62.0 ± 63.2	33.35	121.65	26.5 ± 29.3	3.4 ± 3.7	0.9 ± 1.0	2.2 ± 2.5	3.73 ± 0.04	20.8 ± 0.2
G23.44	2	(0.03, 9.16)	2.00	0.034	33.2 ± 8.6	25.92	54.78	24.1 ± 7.3	5.1 ± 1.6	1.4 ± 0.4	4.4 ± 1.3	2.49 ± 0.07	10.7 ± 0.3
G23.44	3	(-2.88, -3.21)	1.42	0.024	52.9 ± 31.8	18.85	28.00	7.2 ± 4.8	3.1 ± 2.0	0.8 ± 0.5	3.7 ± 2.4	2.90 ± 0.09	8.8 ± 0.3
G23.97S	1	(1.06, 4.22)	2.15	0.029	38.0 ± 10.4	43.37	105.43	25.3 ± 7.9	7.3 ± 2.3	1.9 ± 0.6	7.2 ± 2.3	5.46 ± 0.34	20.2 ± 1.3
G23.97S	2	(-0.60, -7.25)	1.63	0.022	15.9 ± 1.6	9.59	23.73	16.8 ± 2.3	8.4 ± 1.2	2.2 ± 0.3	11.0 ± 1.5	1.67 ± 0.09	4.7 ± 0.3
G25.38	1	(-0.45, 2.15)	1.62	0.026	36.2 ± 9.1	42.94	65.93	23.8 ± 6.9	8.5 ± 2.5	2.3 ± 0.7	9.4 ± 2.7	2.68 ± 0.04	8.9 ± 0.1
G25.38	2	(0.58, 1.33)	1.29	0.021	33.9 ± 4.0	16.87	18.88	7.3 ± 1.0	4.2 ± 0.6	1.1 ± 0.2	5.7 ± 0.8	2.69 ± 0.06	7.1 ± 0.1
G25.38	3	(-1.94, 2.75)	1.45	0.024	28.6 ± 10.3	12.64	18.91	9.0 ± 3.9	4.0 ± 1.7	1.1 ± 0.5	4.9 ± 2.1	2.54 ± 0.04	7.6 ± 0.1
G25.38	4	(-3.77, 3.19)	1.39	0.023	22.1 ± 3.7	11.89	14.75	9.6 ± 2.0	4.7 ± 1.0	1.2 ± 0.3	6.0 ± 1.2	2.40 ± 0.05	6.8 ± 0.1
G25.71	1	(-0.81, -1.07)	1.49	0.041	26.1 ± 6.7	28.47	34.99	53.5 ± 16.8	7.9 ± 2.5	2.1 ± 0.7	5.6 ± 1.7	2.51 ± 0.06	13.0 ± 0.3
G25.71	2	(0.91, -0.47)	1.60	0.044	24.4 ± 4.7	11.04	18.89	31.3 ± 7.4	4.0 ± 0.9	1.1 ± 0.3	2.6 ± 0.6	2.13 ± 0.04	11.8 ± 0.2
G25.71	3	(2.57, 0.09)	1.45	0.040	22.9 ± 2.7	7.82	9.59	17.2 ± 2.5	2.7 ± 0.4	0.7 ± 0.1	1.9 ± 0.3	1.78 ± 0.05	9.0 ± 0.3
BCD configuration observations													
G23.44	1	(0.05, -2.78)	0.92	0.016	63.1 ± 70.1	17.72	33.12	7.1 ± 8.5	7.1 ± 8.6	1.9 ± 2.3	13.2 ± 15.9	3.75 ± 0.05	7.4 ± 0.1
G23.44	2	(-0.97, 10.89)	0.75	0.013	32.5 ± 5.9	10.08	12.57	5.6 ± 1.2	8.6 ± 1.8	2.3 ± 0.5	19.4 ± 4.1	2.44 ± 0.09	3.9 ± 0.1
G23.44	3	(-3.09, -3.44)	1.00	0.017	55.8 ± 45.7	9.06	20.24	4.9 ± 4.4	4.2 ± 3.8	1.1 ± 1.0	7.2 ± 6.4	2.81 ± 0.13	6.0 ± 0.3
G23.44	4	(-0.97, -3.24)	0.90	0.015	34.4 ± 11.7	9.11	16.95	7.1 ± 2.8	7.5 ± 3.0	2.0 ± 0.8	14.2 ± 5.6	3.48 ± 0.06	6.8 ± 0.1
G23.44	5	(0.09, 8.82)	0.98	0.017	32.4 ± 8.6	7.57	21.74	9.8 ± 3.1	8.7 ± 2.7	2.3 ± 0.7	15.1 ± 4.7	2.52 ± 0.07	5.3 ± 0.1
G23.44	6	(0.33, -3.72)	1.11	0.019	58.3 ± 58.7	8.07	23.06	5.4 ± 5.9	3.7 ± 4.1	1.0 ± 1.1	5.7 ± 6.3	3.83 ± 0.06	9.2 ± 0.2
G23.44	7	(-2.16, -2.53)	0.93	0.016	37.8 ± 18.1	8.19	15.51	5.9 ± 3.2	5.8 ± 3.2	1.5 ± 0.8	10.6 ± 5.8	3.13 ± 0.09	6.3 ± 0.2
G23.44	8	(-1.54, 9.44)	0.84	0.014	33.5 ± 6.7	7.31	12.15	5.3 ± 1.2	6.4 ± 1.5	1.7 ± 0.4	12.9 ± 3.0	2.79 ± 0.08	5.1 ± 0.1
G23.44	9	(0.51, 10.26)	0.73	0.012	35.0 ± 9.6	6.65	8.54	3.5 ± 1.1	5.6 ± 1.8	1.5 ± 0.5	13.1 ± 4.2	2.21 ± 0.08	3.5 ± 0.1
G23.44	10	(0.86, -2.51)	0.75	0.013	42.5 ± 21.3	7.13	9.08	3.0 ± 1.7	4.6 ± 2.6	1.2 ± 0.7	10.3 ± 5.9	3.73 ± 0.04	6.0 ± 0.1
G23.44	11	(-0.70, 8.86)	0.76	0.013	32.6 ± 7.2	6.54	10.49	4.7 ± 1.2	6.9 ± 1.8	1.8 ± 0.5	15.5 ± 4.0	2.64 ± 0.08	4.3 ± 0.1
G23.44	12	(-1.84, 5.79)	0.90	0.015	27.1 ± 5.0	5.22	9.05	5.0 ± 1.1	5.3 ± 1.2	1.4 ± 0.3	10.1 ± 2.2	2.47 ± 0.09	4.8 ± 0.2
G23.44	13	(-0.54, -4.29)	0.72	0.012	43.3 ± 34.1	4.85	5.64	1.8 ± 1.6	3.0 ± 2.7	0.8 ± 0.7	7.1 ± 6.3	3.63 ± 0.09	5.6 ± 0.1
G23.44	14	(-0.15, 0.14)	0.77	0.013	34.8 ± 11.9	4.12	5.33	2.2 ± 0.9	3.2 ± 1.3	0.8 ± 0.3	7.0 ± 2.8	3.73 ± 0.03	6.2 ± 0.1
G23.44	15	(1.66, -2.46)	0.82	0.014	32.8 ± 9.7	4.23	7.93	3.5 ± 1.2	4.5 ± 1.5	1.2 ± 0.4	9.3 ± 3.2	3.57 ± 0.07	6.3 ± 0.1
G23.44	16	(0.69, -4.30)	0.74	0.013	57.0 ± 42.8	4.04	5.04	1.2 ± 1.0	1.9 ± 1.5	0.5 ± 0.4	4.3 ± 3.5	4.00 ± 0.08	6.4 ± 0.1
G23.97S	1	(0.94, 4.09)	1.08	0.015	35.9 ± 9.1	19.29	47.91	12.3 ± 3.6	14.1 ± 4.1	3.7 ± 1.1	27.7 ± 8.1	5.58 ± 0.29	10.4 ± 0.5
G23.97S	2	(1.67, 3.99)	0.82	0.011	37.5 ± 12.3	9.90	18.76	4.6 ± 1.7	9.1 ± 3.4	2.4 ± 0.9	23.5 ± 8.8	5.36 ± 0.37	7.6 ± 0.5
G23.97S	3	(0.56, 5.09)	0.86	0.012	54.9 ± 24.5	9.53	17.99	2.9 ± 1.4	5.2 ± 2.5	1.4 ± 0.7	12.8 ± 6.3	4.76 ± 0.29	7.0 ± 0.4
G23.97S	4	(2.15, 5.37)	0.78	0.011	38.3 ± 9.8	4.64	6.15	1.5 ± 0.4	3.2 ± 0.9	0.9 ± 0.2	8.7 ± 2.6	4.96 ± 0.40	6.7 ± 0.5
G23.97S	5	(-0.55, -7.14)	0.86	0.012	16.1 ± 2.9	4.32	6.52	4.5 ± 1.1	8.1 ± 2.0	2.2 ± 0.5	20.2 ± 4.9	1.65 ± 0.10	2.4 ± 0.1
G23.97S	6	(2.03, 3.21)	0.71	0.010	40.2 ± 22.9	4.27	4.84	1.1 ± 0.7	2.9 ± 1.9	0.8 ± 0.5	8.6 ± 5.6	4.65 ± 0.28	5.7 ± 0.3
G23.97S	7	(5.06, -0.80)	0.91	0.012	23.6 ± 6.2	3.86	6.74	2.8 ± 0.9	4.6 ± 1.5	1.2 ± 0.4	10.7 ± 3.5	2.75 ± 0.17	4.3 ± 0.3
G25.38	1	(-0.53, 2.10)	1.19	0.019	36.9 ± 10.5	23.19	73.52	25.9 ± 8.5	17.2 ± 5.7	4.6 ± 1.5	25.8 ± 8.5	2.72 ± 0.05	6.6 ± 0.1
G25.38	2	(-3.51, 3.15)	0.83	0.014	23.2 ± 5.2	11.11	16.52	10.1 ± 2.8	13.9 ± 3.9	3.7 ± 1.0	29.8 ± 8.3	2.45 ± 0.05	4.2 ± 0.1
G25.38	3	(0.81, 1.41)	0.94	0.015	33.6 ± 4.6	6.12	14.81	5.8 ± 0.9	6.2 ± 1.0	1.6 ± 0.3	11.7 ± 1.9	2.71 ± 0.06	5.2 ± 0.1
G25.38	4	(-7.31, 1.91)	0.76	0.012	20.1 ± 3.7	5.85	7.80	5.7 ± 1.3	9.3 ± 2.2	2.5 ± 0.6	21.9 ± 5.1	1.96 ± 0.07	3.0 ± 0.1
G25.38	5	(-1.91, 2.48)	0.74	0.012	29.5 ± 12.5	5.93	7.33	3.4 ± 1.7	5.8 ± 2.9	1.5 ± 0.8	13.9 ± 7.0	2.50 ± 0.04	3.8 ± 0.1
G25.38	6	(0.28, 2.46)	0.70	0.011	36.3 ± 7.1	4.08	4.35	1.6 ± 0.4	3.0 ± 0.7	0.8 ± 0.2	7.6 ± 1.7	2.88 ± 0.05	4.1 ± 0.1
G25.71	1	(-0.66, -1.02)	0.77	0.021	25.1 ± 6.4	25.61	32.77	52.5 ± 16.5	28.9 ± 9.1	7.7 ± 2.4	39.5 ± 12.4	2.51 ± 0.06	6.7 ± 0.2
G25.71	2	(0.27, 6.90)	0.74	0.020	17.1 ± 1.5	5.15	6.25	16.3 ± 2.0	9.7 ± 1.2	2.6 ± 0.3	13.9 ± 1.7	1.25 ± 0.06	3.2 ± 0.1
G25.71	3	(0.67, -0.25)	0.86	0.024	24.7 ± 5.8	3.75	6.03	9.8 ± 2.8	4.3 ± 1.2	1.2 ± 0.3	5.3 ± 1.5	2.16 ± 0.04	6.5 ± 0.1
G25.71	4	(2.06, -0.21)	0.94	0.026	22.1 ± 3.6	3.74	7.94	14.8 ± 3.1	5.5 ± 1.1	1.5 ± 0.3	6.1 ± 1.3	1.84 ± 0.05	6.0 ± 0.2
G25.71	5	(-1.60, -1.23)	0.86	0.024	23.7 ± 5.4	3.87	6.37	10.9 ± 3.1	4.8 ± 1.4	1.3 ± 0.4	5.9 ± 1.7	2.52 ± 0.07	7.5 ± 0.2
G25.71	6	(-0.69, -0.14)	0.73	0.020	24.9 ± 6.5	3.90	4.37	7.1 ± 2.3	4.3 ± 1.4	1.2 ± 0.4	6.2 ± 2.0	2.43 ± 0.04	6.2 ± 0.1